










# Machine Learned Interatomic Potentials for Ternary Carbides trained on the AFLOW Database

Josiah Roberts <sup>1</sup>, Biswas Rijal <sup>1</sup>, Simon Divilov <sup>2,3</sup>, Jon-Paul Maria <sup>4</sup>, William G. Fahrenholtz <sup>5</sup>,  
Douglas E. Wolfe <sup>4</sup>, Donald W. Brenner <sup>6</sup>, Stefano Curtarolo <sup>2,3</sup> and Eva Zurek <sup>1,\*</sup>

<sup>1</sup>Department of Chemistry, State University of New York at Buffalo, Buffalo, NY 14260, USA

<sup>2</sup>Department of Mechanical Engineering and Materials Science, Duke University, Durham, NC 27708, USA

<sup>3</sup>Center for Autonomous Materials Design, Duke University, Durham, NC 27708, USA

<sup>4</sup>Department of Materials Science and Engineering, The Pennsylvania State University, University Park, PA 16802, USA

<sup>5</sup>Department of Materials Science and Engineering, Missouri University of Science and Technology, Rolla, MO 65409, USA

<sup>6</sup>Department of Materials Science and Engineering, North Carolina State University, Raleigh, NC 27695, USA

Large density functional theory (DFT) databases are a treasure trove of energies, forces and stresses that can be used to train machine learned interatomic potentials for atomistic modeling. Herein, we employ structural relaxations from the AFLOW database to train moment tensor potentials (MTPs) for four carbide systems: HfTaC, HfZrC, MoWC and TaTiC. The resulting MTPs are used to relax  $\sim 6300$  random symmetric structures, and are subsequently improved via active learning to generate robust potentials (RP) that can relax a wide variety of structures, and accurate potentials (AP) designed for the relaxation of low-energy systems. This protocol is shown to yield convex hulls that are indistinguishable from those predicted by AFLOW for the HfTaC, HfZrC and TaTiC systems, and in the case of the CMoW system to predict thermodynamically stable structures that are not found within AFLOW, highlighting the potential of the employed protocol within crystal structure prediction. Relaxation of over three hundred  $\text{Mo}_{1-x}\text{W}_x\text{C}$  stoichiometry crystals first with the RP then with the AP yields formation enthalpies that are in excellent agreement with those obtained via DFT.

## INTRODUCTION

Machine learned interatomic potentials (ML-IAPs), which are trained on density functional theory (DFT) data, have irrevocably changed the way in which computational materials science is carried out. They have increased the complexity of the systems that can be studied via static calculations [1], the duration of molecular dynamics trajectories [2], and made it possible to routinely model effects, such as anharmonicity [3], which are commonly neglected due to the large computational cost associated with the requisite DFT calculations. Moreover, they are becoming increasingly important in the field of crystal structure prediction (CSP) where it may be necessary to relax hundreds or thousands of structures to find the global minimum and a handful of low-lying local minima [4]. As CSP methods tackle systems with increased combinatorial complexity such as ternaries and quaternaries [5], it is becoming increasingly important to develop protocols that can be used to train and employ ML-IAPs for CSP.

Some of the most well-known ML-IAPs include neural networks (NNs) [6, 7], the spectral neighbor analysis potential (SNAP) [8], moment tensor potentials (MTPs) [9], the Gaussian approximation potential (GAP) [10], and, more recently ultra-fast (UF) [11], and ephemeral data-derived (EDD) potentials [12]. Provided an ML-IAP can accurately describe the potential energy surface (PES) of a multi-component system, it can significantly accelerate a CSP search while at the same time enabling exploration of wider regions of compositional space [4]. Indeed, recent algorithmic developments have shown promising results: CSP methods including random and evolutionary searches, as well as particle swarm optimization have been coupled with various ML-IAPs and applied to predict crystalline structures of boron [13–15], carbon [14, 16], sodium [14], phosphorus [17], lithium [18] as

well as Mg-Ca [19] and various metal-tin [20, 21] alloys at 1 atm and under pressure. For ternary crystalline systems, early work showed that adaptive classical potentials can accelerate CSP in the Mg-Si-O system [22], and recently ephemeral deep learning potentials combined with random searching have been used to predict candidate structures for a reported Lu-N-H superconducting phase [23], and  $\text{Zn}(\text{CN})_2$  metal-organic-frameworks [24].

A challenge in developing ML-IAPs for CSP is that they need to be able to predict the energies of unstable structures, as well as those that are close to the local minima in the PES. Moreover, because ML-IAPs are poor at extrapolation, they cannot accurately predict the energies (or forces or stresses) of configurations that differ significantly from those they have seen before. Traditionally, DFT data sets containing thousands to hundreds-of-thousands of structures have been generated for the training and testing of ML-IAPs [14, 25]. A wide range of procedures have been employed to create these DFT data sets including generating structures randomly [14], perturbing the geometries of such structures via ‘shaking’ [12], *ab initio* molecular dynamics runs at various temperatures [26], decorating predefined lattices with atoms of different types while simultaneously varying the chemical composition [25], relaxation of structures generated via constrained evolutionary searches [7], straining crystal lattices, creating defect structures, and more [26, 27].

Unfortunately, even when large DFT data sets are employed for training, it is unlikely that the resulting ML-IAPs can predict, with sufficient accuracy, the energies of the various structures encountered in the course of a CSP run. One strategy that has been proposed for the generation of a multi-purpose ML-IAP, given a limited number of DFT calculations, relies on the automatic iterative building of the fitting database by selecting the most diverse structures [28]. Additional techniques include various active learning [29, 30] and learning-on-the-fly [31] methods, where the potential is updated and improved during the course of the search. It has been suggested that active learning could be used to generate two ML-IAPs: a ro-

\* ezurek@buffalo.edu

bust one that is able to optimize any structure the CSP algorithm encounters and make rough predictions, and an accurate one trained on (and able to relax) only the low-energy structures [14, 25].

ML-IAP based simulations where the potential is updated on-the-fly may be initialised using either an empty/untrained potential [25], or one that has been pre-trained. The former strategy may require just as many, if not more, DFT evaluations than the latter because the likelihood of encountering a configuration that is deemed extrapolative is high, necessitating a retraining of the ML-IAP [14]. Thus, there appears to be ‘no-free-lunch’ since the construction of a reliable ML-IAP requires numerous expensive DFT calculations. At the same time, a large number of databases exist – AFLOW (Automatic FLOW) [32–34], the Materials Project (MP) [35], the Open Quantum Materials Database [36], etc. – each containing millions of DFT evaluations of the energies, forces and stresses of extended systems. Furthermore, it is becoming standard practice for researchers to deposit the DFT data generated during the course of a computational project in repositories such as NOMAD [37], OCELOT [38] and NIST Materials Data [39]. One way this data is being used is to train ML-IAPs for the computational study and exploration of the vast PES of all possible chemistries. Some of the forefront examples of such ‘universal’ ML-IAPs, which can predict energies, forces and stresses using equivariant graph neural networks, include M3GNet [40], CHGNet [41], ALIGNN-FF [42], MACE-MP-0 [43], and GNoME [44].

The training of potentials on already existing DFT-data is illustrated here by combining outputs present within the AFLOW [32] database with MTPs [9], as implemented within the Machine Learned Interatomic Potentials (MLIP) program [45]. Specifically, chemically sensible structures, which are randomly selected from the relaxation trajectories stored within the AFLOW database, are used to train an MTP that is subsequently employed to relax a large number of random symmetric structures spanning a wide composition range. In contrast to the recently developed universal ML-IAPs [40–44, 46], here we only train on a subset of the data found within AFLOW, chosen for the application in-mind. Therefore, the ML-IAPs developed here are system-specific, and not universal. What distinguishes our study from prior works [7, 12, 14, 26, 27] is that rather than generating our own DFT-training set, we employ already existing data found within AFLOW. In a further step, the AFLOW-trained potentials are improved via active learning, generating ML-IAPs that can be robust (able to roughly optimize any configuration) or accurate (for the optimization of only low-energy structures near the convex hull). Thus, only a small number of supplementary DFT calculations are required to develop system-specific MLIPs that enable the computational exploration of evermore complex PESs towards the discovery of materials.

A utility package that automates this training process, the *Plan for Robust and Accurate Potentials* (PRAPs), is described. The method is used to determine the zero-Kelvin phase diagrams of four ternary metal carbides, chosen because they represent materials with superlative mechanical properties [47, 48]. The PRAPs generated convex hulls whose lowest

energy structures are optimised with DFT are in good agreement with the DFT-relaxed AFLOW hulls. Moreover, in the case of the CMoW system, thermodynamically stable structures are found that are not present in the AFLOW data. Further calculations with the accurate potential find a variety of  $\text{Mo}_{1-x}\text{W}_x\text{C}$  stoichiometry phases at/near the tie-line indicating the possibility of a solid-solution with a very low miscibility gap critical temperature.

## RESULTS AND DISCUSSION

### A. Plan for Robust and Accurate Potentials (PRAPs)

We created MTPs of varying complexity for a number of ternary metal carbides and investigated their capabilities to predict structures outside of their training sets. Our choice of MTPs was motivated by their excellent balance between model accuracy and computational efficiency [26, 49], their application towards multicomponent systems [25, 27, 50–52], their ability to predict phonons and thermodynamic properties, [3, 53, 54] and the availability of a powerful active learning scheme (ALS) that has been interfaced with the MTP method [25, 55].

The MLIP software package trains MTPs and uses them to relax the geometries and minimize the energies of a wide variety of chemical systems [45]. The simplest form of training, basic training, employs the energy, force and stress (EFS) data of a set of configurations, as obtained from DFT or other quantum chemical calculations, to generate an MTP. The complexity of the MTP is described by a user-selected *level*, a notation containing information about the number of basis functions and parameters comprising the potential. The ALS employs a D-optimality criterion to calculate the extrapolation degree or grade,  $\gamma$ , for every structure that is generated throughout the course of the simulation (relaxation trajectory or molecular dynamics run) [25, 55]. MLIP automatically selects configurations to be added to the training set if their  $\gamma$  falls within a user-defined range; we choose the default  $2 < \gamma \leq 10$ . The calculation (relaxation or molecular dynamics run) is terminated if  $\gamma$  exceeds the upper bound, triggering retraining of the MTP, and the procedure repeats until the simulation finishes with  $\gamma \leq 10$ . Further information about MTPs, including their functional form, the quantities included in the cost function, and details of the active learning procedure are provided in Section S1 of the Supplementary Information.

In what follows we give a brief overview of the PRAPs utility package employed in this study; a forthcoming manuscript will describe its composition and usage. PRAPs interfaces with MLIP and automates the creation of a Robust Potential (RP) and Accurate Potential (AP) using the aforementioned ALS, and employs basic training for supplemental tasks. From a given a set of configurations obtained from AFLOW, a subset of  $\sim 800$  configurations is chosen randomly and used to train an MTP (Figure 1, gray box). This procedure is repeated five times, generating five different MTPs (as recommended in the MLIP manual [45]), mimicking a cross-validation procedure. From these PRAPs finds the ‘best’ MTP, defined as the

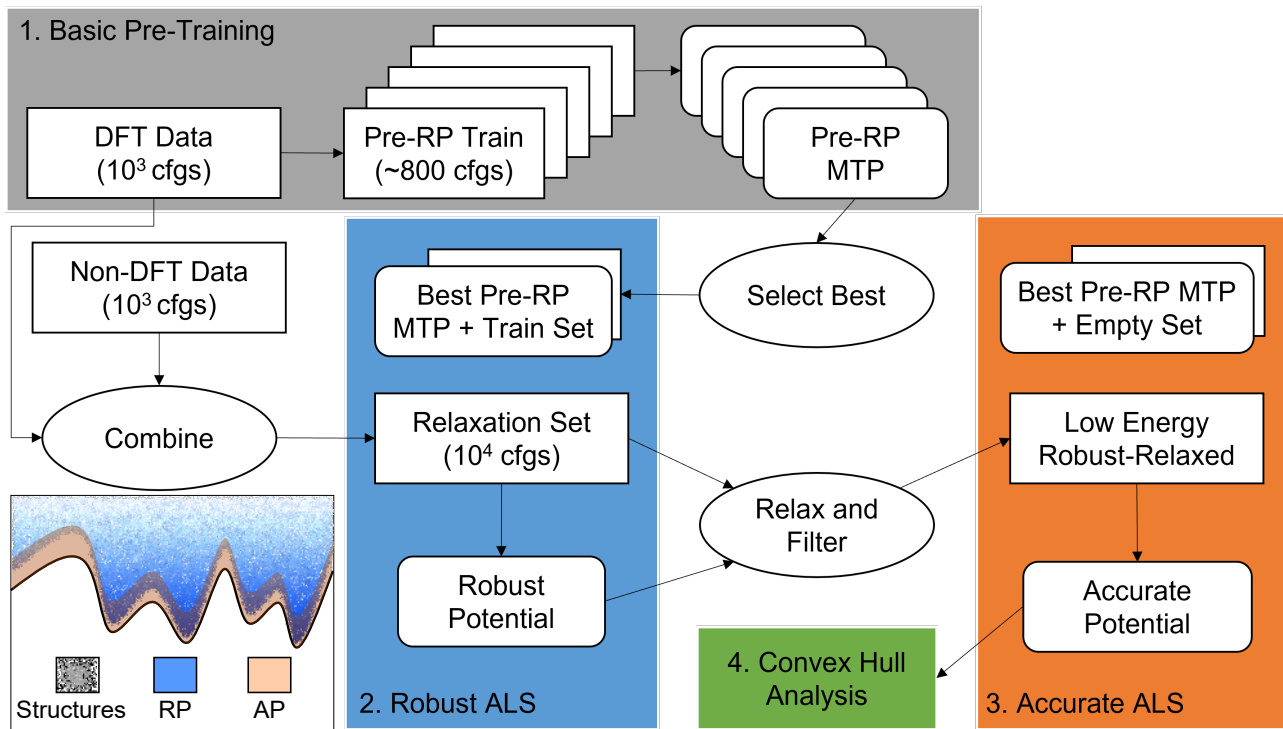


FIG. 1. Workflow in the *Plan for Robust and Accurate Potentials* (PRAPs) package, which automates the generation of a moment tensor potential (MTP), given any quantum mechanical training set (here the online AFLOW database [32]). Five MTPs are trained on a set of configurations (cfgs) and the best (the pre-Robust Potential, pre-RP) is chosen (gray box). The pre-RP is employed to initialise the training of a RP via an active learning scheme (ALS, blue box). The RP is generated by relaxing the configurations comprising the Relaxation Set. The RP-relaxed lowest energy configurations are chosen (filtration step) to train an Accurate Potential (AP) via active learning (orange box). The AP-relaxed structures may be sent for relaxation via AFLOW-DFT, followed by subsequent analysis (green box). The inset schematically illustrates the energy distribution of the structures that can be relaxed with the RP and the AP. Optionally, structures generated using such a procedure may not be exact since the intermediate structures in a DFT relaxation trajectory may have erroneous energies or forces resulting from Pulay stress that arises when the lattice vectors are varied. another procedure (here RANDSPG [56]), labelled as ‘Non-DFT Data’, may be relaxed via the RP and/or the AP, and this auxiliary set of structures also comprises the Relaxation Set. Rectangles with sharp (curved) corners represent structural data (potentials).

one that identifies the most high-and-low-energy structures (ten of each are compared), or if multiple MTPs fulfill this criteria, the MTP with the lowest root-mean-squared (RMS) training error. This step is intended to mitigate the initial random parameters that MLIP assigns at the beginning of training, but users may bypass it if they so desire. To ensure that training is performed on sensible structures, PRAPs can filter out configurations with undesirable interatomic distances (default), or cell volumes. If relaxation trajectories comprise the data set, dozens of ionic steps originating from the same system may be present. Though using many similar configurations for training may be beneficial in some cases, in others it may be desirable to exclude the intermediate steps and only include the final relaxed configuration, and PRAPs provides an option for users to select the desired behaviour.

The RP training (Figure 1, blue box) begins using the PRAPs-determined ‘best’ MTP. The set of configurations may be optionally augmented with structures lacking any EFS data (Figure 1, left-hand-side, no box), which are combined with the initial DFT data set to form the relaxation set. The relaxation set is used to train the RP by active learning. The active

learning begins with the ‘best’ training set and MTP from the pre-training step (if performed, otherwise PRAPs trains from scratch). During the active learning process, the relaxation set is relaxed using MLIP’s built-in functionality and new structures are added to the training set based on the D-optimality criterion (a detailed discussion of this step is available in Section S1). The final output is a potential capable of performing a reasonable relaxation of most any configuration in the relaxation set.

After relaxation with the RP, PRAPs filters out structures with energies above a specified cutoff (default 50 meV/atom) for each composition present. This creates the ‘Robust Relaxed’ set, which is employed to train the AP via active learning (Figure 1, orange box). The procedure for training the AP is similar to the RP except that PRAPs begins with an empty training set instead of the ‘best’ pre-trained MTP’s training set. We find that this results in better predictions as the AP should not see non-ground-state structures during training. The resulting AP should improve the EFS predictions for these low-energy structures. For additional efficiency, users can alter the convergence criteria of the AP training at the cost of a few

meV/atom in the training error (as described more thoroughly below).

PRAPs performs a number of analyses throughout and at the end of the training procedure. In addition to calculating the training and prediction RMSE and mean absolute error (MAE), and comparing the ten high-and-low-energy structures, it can generate a set of convex hull candidates, invoke AFLOW [32, 57] to relax them, and use this data to generate composition-energy convex hull plots (Figure 1, green box). Finally, PRAPs contains a checkpoint system to allow users to start or re-start a job from a certain step. PRAPs is primarily a project management software that performs and automates many menial tasks, and generates plots that may be desired, thereby reducing the amount of human time required to generate MTPs for a particular system and analyze their performance.

In what follows we seek to answer two questions using PRAPs: (i) Can already existing quantum-mechanical data be used to train an MTP that is able to reproduce the DFT-calculated convex hull for a particular ternary alloy? (ii) And, can we use these MTPs to discover thermodynamically stable structures comprising the convex hull that are not present in the DFT-training set? In what follows, we show the answers to both questions is ‘yes’.

## B. Machine Learned Interatomic Potentials from AFLOW Data

To illustrate how already-existing DFT results can be scraped from large databases and repurposed towards the generation of system specific MLIPs, we chose four ternary alloy systems: CHfTa, CHfZr, CTaTi, and CMoW. TaC, HfC, ZrC, and TiC all adopt the rocksalt structure and are refractory ceramic materials with desirable mechanical properties [58]. Though MoC can adopt the same rocksalt structure under pressure [59], at ambient conditions MoC and WC prefer a hexagonal arrangement instead [60]. For nearly a century the propensity for transition metal carbides to form high-melting point solid solutions with compositions such as  $\text{Hf}_{1-x}\text{Ta}_x\text{C}$  has been known [61, 62]. The metal formulation can be engineered to contain multiple atoms, and when there are five or more metals, the configurational entropy stabilizes single-phase high entropy carbides (HECs) [47, 63, 64] and their thin films [48]. Recently, ML-IAPs have been developed for various HECs including a deep learning potential for  $(\text{ZrHfTiNbTa})\text{C}_5$  [65] and a low rank potential for  $(\text{TiZrNbHfTa})\text{C}_5$  [66]. Herein, we illustrate that data found within AFLOW, coupled with active learning, can be used to train MTPs for ternary carbides, with the future goal of HECs in mind.

For training we employed DFT relaxation trajectories of  $\sim 210$  structures obtained from the AFLOW database, which have been generated through a combination of structure prototyping of naturally occurring compounds [67–69] and structure enumeration algorithms [70], followed by relaxation using density functional theory. This resulted in  $\sim 5500$ – $6000$  in-

System	AFLOW structures	Configurations	RANDSPG structures
CHfTa	209	6064	6346
CHfZr	210	5811	6356
CMoW	210	5524	6338
CTaTi	211	5831	6347

TABLE I. Number of unique structures for the studied ternary carbides found within the AFLOW database, and the number of individual ionic steps (configurations) from their structural relaxations. The number of individual structures generated by RANDSPG that were employed to develop the robust and accurate potentials using the MLIP program package are also provided.

dividual configurations on which the MTP was trained (Table I). From this training set,  $\sim 800$  configurations, with a minimum interatomic distance greater than  $1.1 \text{ \AA}$ , were chosen randomly and MTPs of levels 10, 16 and 22 were trained in the “basic” mode. For the CMoW system, no level 22 data is reported due to the excessive computational cost required to obtain well-trained potentials. Five trainings were performed, and the best potential was chosen as the pre-Robust Potential (pre-RP). As expected, the training errors for the pre-RP (Table S1) decreased with increasing MTP level, with the average MAE (RMSE) on the energies being 27 (44), 16 (25) and 8 (13) meV/atom, and for the forces being 75 (217), 51 (147) and 26 (78) meV/Å for levels 10, 16 and 22, respectively. Comparison of the ten highest and ten lowest energy structures as predicted by DFT and the pre-RP revealed that the MTP rarely miscategorized the structures, but had difficulty correctly categorizing more than 7 in the correct highest or lowest energy set (Table S2).

Previous studies have suggested that when used for CSP, MTPs should be trained on a very diverse set of structures [14, 25], and as Table I shows, the original AFLOW data was somewhat limited. To obtain this diversity, we used the RANDSPG [56] program to create crystal lattices with up to eight atoms in the unit cell, for all possible ternary compositions. Lattice vectors were constrained to fall between  $3$ – $10 \text{ \AA}$ , and unit cell volumes between  $200$ – $600 \text{ \AA}^3$ , with a minimum interatomic distance of  $1.1 \text{ \AA}$ . For each ternary system,  $\sim 6300$  structures were generated (Table I) and combined with the initial AFLOW data to form the relaxation set (Figure 1) used in training the RP.

For a given stoichiometry RANDSPG determines the compatible spacegroups, based upon the Wyckoff positions, and randomly chooses one prior to decorating its sites with atoms, thereby enabling the creation of random symmetric crystal lattices. Employing symmetric structures in the first generation of an evolutionary or particle-swarm directed CSP search greatly decreases the number of configurations that need to be optimized to locate the global minimum in the PES. This can be understood by noting that symmetric structures tend to be either very stable or unstable, spanning a greater amount of the potential energy hypersurface than those generated without symmetry constraints [5]. Indeed, tests have shown that the average energy of random structures that are symmetric is higher (less negative) than those that are purely random [56].



Alloy	Energy Errors (meV/atom)		Force Errors (meV/Å)	
Level 10	Robust Potential	Accurate Potential	Robust Potential	Accurate Potential
CHfTa	45 (75)	24 (36)	89 (281)	82 (270)
CHfZr	53 (87)	37 (62)	81 (255)	57 (170)
CMoW	71 (125)	71 (93)	120 (377)	50 (160)
CTaTi	51 (85)	53 (70)	99 (303)	76 (220)
Level 16	Robust Potential	Accurate Potential	Robust Potential	Accurate Potential
CHfTa	42 (72)	29 (90)	79 (238)	53 (169)
CHfZr	43 (77)	22 (30)	68 (211)	42 (112)
CMoW	68 (118)	168 (214)	113 (359)	96 (276)
CTaTi	41 (60)	45 (59)	90 (285)	56 (161)
Level 22	Robust Potential	Accurate Potential	Robust Potential	Accurate Potential
CHfTa	44 (70)	21 (57)	85 (270)	23 (71)
CHfZr	39 (62)	29 (91)	61 (197)	18 (59)
CTaTi	36 (58)	82 (218)	73 (223)	25 (79)
Level 16*	Robust Potential	Accurate Potential	Robust Potential	Accurate Potential
CHfTa	156 (126)	16 (19)	129 (381)	50 (150)
CHfZr	107 (78)	24 (37)	93 (278)	40 (114)
CMoW	155 (97)	67 (120)	108 (336)	52 (196)
CTaTi	153 (119)	92 (112)	110 (345)	45 (134)

\*Calculations performed without pre-training the MTP on the AFLOW data (grey box in Figure 1).

TABLE II. Prediction errors for energies (meV/atom) and forces (meV/Å) by system, level, and potential. Each box contains the mean-absolute-error and, in parentheses, the root-mean-squared errors (RMSE). Only the Robust Potential (RP) and the Accurate Potential (AP) developed during the active learning scheme (ALS) as illustrated in Figure 1 are shown here; data for the pre-Robust Potential can be found in the SI. The training errors for each potential reflect the RMS values obtained by comparing the energies of that potential’s training set as obtained by single-point DFT calculations against those predicted by the respective potential. The prediction errors for the RP indicate comparison of the energies of the original AFLOW data with the energies predicted by the respective potential. The prediction errors for the AP indicate comparison of only the low-energy AFLOW structures with those predicted by the respective potential.

Table II provides the prediction errors for the energies and forces for both the RP and the AP for different MTP levels. Determining the prediction error when such active learning schemes are used is complicated by the fact that each level of theory (DFT or MTP level) will encounter different structures during the relaxation process. While it is possible to predict the energy of every structure comprising the AFLOW relaxation trajectories via the RP or the AP, such a procedure is fraught with difficulties because of the noise in the DFT relaxation trajectory data. Specifically, the relaxation trajectory may have erroneous energies, forces and stresses resulting from a change in the planewave basis as the lattice vectors are varied during the course of the optimization. Moreover, the AFLOW data contained a few configurations whose magnitude of per-atom-energies were substantially larger than others, though they survived the distance-filtering-criteria (Supplementary Figure 1. Therefore, in Table II we have opted to compare the DFT energies and forces on the final AFLOW relaxed structures, which are accurately calculated, against their RP and AP predicted values.

A number of trends can be observed from examination of Table II. First, the MAE are notably smaller than the RMSE, suggesting the presence of poorly-predicted outliers. The prediction errors with the RP generally decrease with increasing

level of MTP, but the MAE do not fall below 40 meV/atom for energies and 60 meV/Å for the forces. While these errors might seem large compared to the  $< 4$  meV/atom and  $< 160$  meV/Å RMSEs computed for single-component systems wherein the testing and training dataset contained structures that could be derived via perturbations of the ground state crystal [26], they are in-line with some of the errors presented in Ref. [27] that trained MTPs for Li-Al alloys and applied them to a broad range of compositions and crystal lattices. In Ref. [25] the only errors reported for the Al-Ni-Ti system were for the training set with MAEs (RMSEs) of 18 (27) meV/atom for the RP and 7 (9) meV/atom for the AP. In Ref. [14] a RP yielded a training RMSE of 170 meV/atom for allotropes of boron, and an AP yielded errors of 11 meV/atom for the 100 lowest-energy structures that were found.

A key difference between the workflow presented here as compared to previous work by Gubaev and co-workers [25] is the pre-training step on the AFLOW data. To test what effect this may have, we performed the PRAPs procedure starting from an empty MTP, that is one that had not been trained on AFLOW data for a level 16 MTP. Therefore, the basic pre-training denoted schematically in the grey box in Figure 1 was not performed. Table II clearly illustrates that the MAEs for the energies were significantly improved by the AFLOW pre-

training, and the RMSEs were slightly improved (by 94 and 16 meV/atom, on average).

A common practice in CSP is to use less accurate, but quicker methods to estimate the energies of a large number of structures, and then to optimize those with low energies with progressively more accurate, but costlier, methods. This workflow saves computational expense by filtering out structures that are unlikely to be stable prior to performing calculations that yield a more predictive rank order. A similar strategy was employed in Refs. [25] and [14] where both robust and accurate MTPs were trained for CSP. In addition to generating 375,000 binary and ternary bcc, fcc and hcp-type unit cells, 1463 Al-Ni-Ti ternary structures were created via decorating prototypes [25]. It was noted that the prototype-derived structures might possess geometries that were not chemically sensible because of short metal-metal distances and too-small volumes, which could lead to large MTP prediction errors. To circumvent this problem, structures with formation energies (as determined with a Robust MTP) that were within 100 meV/atom of the convex hull were chosen for re-relaxation using active learning starting from an empty MTP to generate an AP. In another related work, the large training error of 170 meV/atom obtained in a CSP search performed on boron, which has a very complex PES, prompted the authors to retrain the MTP on low-energy structures so it could accurately predict their energies [14].

Similar to these two studies [14, 25], our RANDSPG generated structures span a wide energy range. Although the RPs obtained from including them in the training set have large errors, they are able to correctly identify most low-energy configurations, and not misidentify them as having high energies. Therefore, by choosing the RP-relaxed structures whose energies were within 50 meV/atom of the minimal energy structure for each composition, we can curate a new set of training data that can then be used to create an AP. Because the low-energy structures are expected to be better behaved than the full relaxation set, possessing nearly optimized geometries that are chemically sensible, the AP should yield lower training and prediction errors than the RP.

In many cases both the training and prediction RMS errors obtained for the AP decreased with increasing MTP level, however they did not fall below 50 meV/atom. Considering that most high-throughput and CSP searches are performed in a stepwise procedure, at each level filtering undesirable structures prior to increasing the accuracy by which the remaining subset is treated, this error is acceptable. Indeed, in both Refs. [25] and [14] all structures with sufficiently low energy, as predicted by the AP, were re-optimized with DFT to obtain an improved energy ordering. Similarly, in CSP searches on Lu-N-H [23] and  $\text{Sc}_x\text{H}_y$  [24] the lowest energy structures, as predicted by an ML-IAP, were relaxed with DFT to determine a more accurate energy rank.

For an MTP level of 22, the training in some cases took substantially longer than at lower levels. The reason for this is that the ALS, as originally designed [55], terminates when MLIP does not find any configurations that need to be added to the training set. Here a different protocol was used, where the active learning for the AP was stopped when the number

of structures to be added to the training set was less than 1% of its size. This choice was motivated by the observation that at times fewer than ten configurations were being added to a training set of thousands in a single iteration, which took a full day to process, for a gain in RMS training error that was  $< 1$  meV/atom. Tests showed that the choice of a variety of early termination criteria (which can be chosen as options in PRAPs) comes at the cost of 2-5 meV/atom in training error.

A key question to be answered is: “Does the ML-aided procedure reduce the total computational expense?” For each ternary the AFLOW and RANDSPG datasets contained  $\sim 210$  and  $\sim 6300$  individual structures, respectively (Table I). Therefore,  $\sim 6500$  geometry optimizations would be needed to relax all of these configurations. Using MTPs, a maximum number of single point DFT energy evaluations performed during the course of the training was  $\sim 3000$  (Figure 2) for the CTaTi system at level 22. Dividing the number of configurations comprising the AFLOW data by the number of structures gives an average estimate of the number of steps required per geometry optimization ( $\sim 28$ ). Thus, our protocol reduces the number of DFT evaluations that would need to be performed to relax all of the considered structures by a factor of  $\sim 30$  or more (as high as 180 for the CHfTa system at an MTP level of 10). We note that as MTP level increases, the number of single-point calculations increases (as does the total training time), as expected (*e.g.* see Table 3 in Ref. [45]). The reason for this is that higher level MTPs contain more parameters, and therefore require more training data to fit these parameters.

Finally, we consider a few miscellaneous points about the setup and training procedures. Since the training data was predominantly for cubic structures, the HEAs which inspired our choice of elements typically crystallize in a cubic manner [47, 48], and the ternary carbides considered herein assume either cubic or hexagonal lattices, it is fair to ask if the results could be improved if the RANDSPG structures were generated using only spacegroups with these symmetries. A test on all four systems, at an MTP level of 10, revealed that both training and prediction errors were very similar when using a reduced set of  $\sim 200$  RANDSPG structures across only HCP, FCC, and BCC-type unit cells in addition to the AFLOW data (Table S3). A reader may ask why the pre-training step is carried out here since active learning can be performed on an empty training set [14, 25, 45]. Another test on CHfTa at level 10, showed that omitting the pre-training step resulted in a savings in time at the cost of training and prediction error (Table S4). The user can keep these trade-offs in mind when designing the computational protocol to be employed for their specific situation.

### C. Predicted Convex Hulls

Let us now examine the convex hulls and investigate the structures that PRAPs relaxed with the robust and accurate potentials. Since optimization of random symmetric configurations is the first step in CSP, we examined if the aforementioned workflow could discover lattices not found within AFLOW whose energies lie on, or close to the convex hull. We

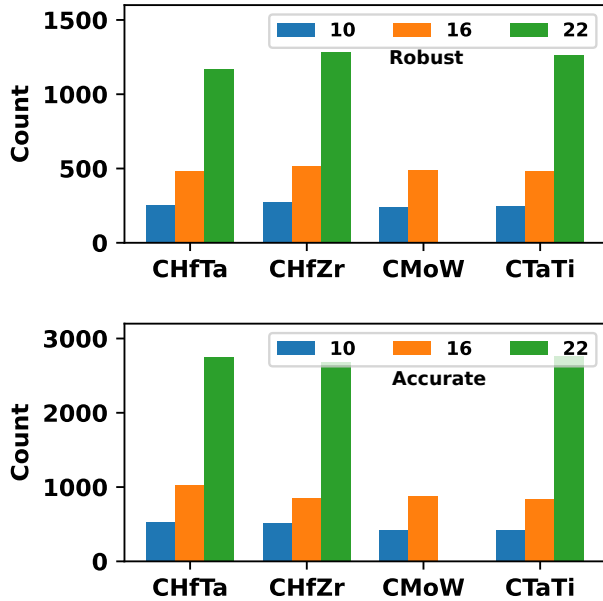


FIG. 2. Number of density functional theory (DFT) single point energy evaluations performed during the generation of the robust (top) and accurate (bottom) potentials according to the procedure illustrated in Figure 1 for each ternary carbide system at a particular MTP level (see legend).

filtered out the AP predicted configurations that were within 50 meV/atom of the lowest energy structure for each composition and DFT-relaxed them via AFLOW. The resulting geometries were then concatenated with the fully relaxed AFLOW data to produce convex hulls, for different MTP levels (Figure 3 and Figures S9 and S10).

The data found within AFLOW for the CHfTa, CHfZr, and CTaTi systems all contained multiple compounds on or near the convex hull with the  $M_{1-x}N_xC$  stoichiometry ( $x = 0.25, 0.33, 0.5, 0.67, 0.75$ ) (Figures S3-S13). Examination of these structures suggested that they could all be obtained via relaxation of metal-carbide rocksalt structures whose metal sites were decorated with two different types of atoms, as would be expected for a solid-solution. On the other hand, for the CMoW system, AFLOW did not contain any ternary carbide phases with a  $Mo_{1-x}W_xC$  composition that were on the hull (Figure 3). Unlike the cubic binary carbides comprised of metal atoms from group 5 or 6, isostructural MoC and WC (Figure 4(a)) adopt the hexagonal  $P\bar{6}m2$  (#187) space-group, suggesting that  $Mo_{1-x}W_xC$  stoichiometry structures would be hexagonal as well. Examination of a  $Imm2$  symmetry  $Mo_{0.5}W_{0.5}C$  phase that was 17 meV/atom above the convex hull (teal dot in Figure 3) showed that it could not be derived from a decoration of a hexagonal metal-carbide lattice. Instead, it was related to a high-pressure phase of GaAs (AFLOW prototype [AB\\_o14\\_44\\_a\\_b](#)) where the Ga atoms were replaced by C, half of the As atoms were substituted by Mo, and the other half by W.

In addition to the elemental endpoints, as well as MoC and WC, cubic MoW and rhombohedral  $C_2Mo_4$  (Figure 3) comprise the AFLOW convex hull for the CMoW system. Tetragonal  $Mo_{14}W_2$  (labelled by a purple dot) lies 1 meV/atom above the hull – a value that is within the error of the  $k$ -mesh and kinetic energy cutoffs employed in our planewave calculations. A different choice of DFT functional, inclusion of zero point energy or finite temperature contributions may place this structure on the hull. We then examined if MTPs trained by PRAPs on AFLOW data could relax structures created with RANDSPG and identify other thermodynamically stable compounds, not found within AFLOW for the CMoW system.

We compare the AFLOW hull with hulls predicted using the PRAPs procedure (Figure 3 and Figures S9 and S10). At an MTP level of 10 no additional structures emerged, and the PRAPs-derived hull was identical to the one found within AFLOW. However, for an MTP level of 16, additional thermodynamically stable structures were found, including  $Imm2$   $Mo_{0.75}W_{0.25}C$ , in addition to the on-and-near-hull compounds present in AFLOW. The  $Imm2$  phase, containing two formula units per primitive cell, resembles hexagonal MoC except that in every second layer half of the metal atoms are replaced by W, and the substituted metal-containing triangular nets are arranged in an  $\cdots ABAB \cdots$  stacking sequence with respect to each other (Figure 4(b)). This phase likely originated from the RANDSPG set, which was subsequently optimized, in an active learning sense, via the robust and accurate potentials. When an MTP of level 10 was used instead,  $Imm2$   $Mo_{0.75}W_{0.25}C$  was not on the convex hull likely because the relaxation process with the robust potential pushed this particular configuration too high in energy. To test this hypothesis the level 16 data for  $Imm2$   $Mo_{0.75}W_{0.25}C$  was concatenated with the structures that are present on the level 10 hull, and further analysis revealed that this phase was predicted to be thermodynamically stable.

In addition, four more structures, within 1 meV/atom of the convex hull, lay on the level 16 hull:  $P\bar{6}m2$   $Mo_{0.5}W_{0.5}C$ ,  $P\bar{6}m2$   $Mo_{0.333}W_{0.666}C$ ,  $P\bar{6}m2$   $Mo_{0.666}W_{0.333}C$  and  $Cm$   $Mo_{0.25}W_{0.75}C$  (Figure 4(c-f)). Though the first has the same composition as the structure present within AFLOW, it is 17 meV/atom lower in energy. In fact, if we do not distinguish between the identities of the metal atoms, the AFLOW structure can be transformed into  $P\bar{6}m2$   $Mo_{0.5}W_{0.5}C$  by doubling it along the  $b$ -axis followed by three sets of translations of various subsets of atoms. In both phases the C atoms fall within trigonal-prismatic holes, but in this particular structure the triangular (and square) faces all point along the same crystallographic direction, while in the AFLOW structure half of the prisms are rotated, thereby swapping the axes along which the two sets of faces lie. Importantly, PRAPsfound  $P\bar{6}m2$   $Mo_{0.5}W_{0.5}C$  corresponds to a coloring of the hexagonal CMo/CW prototype structure with an  $\cdots ABAB \cdots$  arrangement for the metal-containing hexagonal nets (Figure 4(c)). Similarly, the remaining three PRAPsfound structures can be derived from colorings of the hexagonal parent phase, with  $P\bar{6}m2$   $Mo_{0.333}W_{0.666}C$  and  $P\bar{6}m2$   $Mo_{0.666}W_{0.333}C$  being inverses of each other, while  $Cm$   $Mo_{0.25}W_{0.75}C$  can be described as a W-rich  $\cdots ABAB \cdots$  layered decoration of this

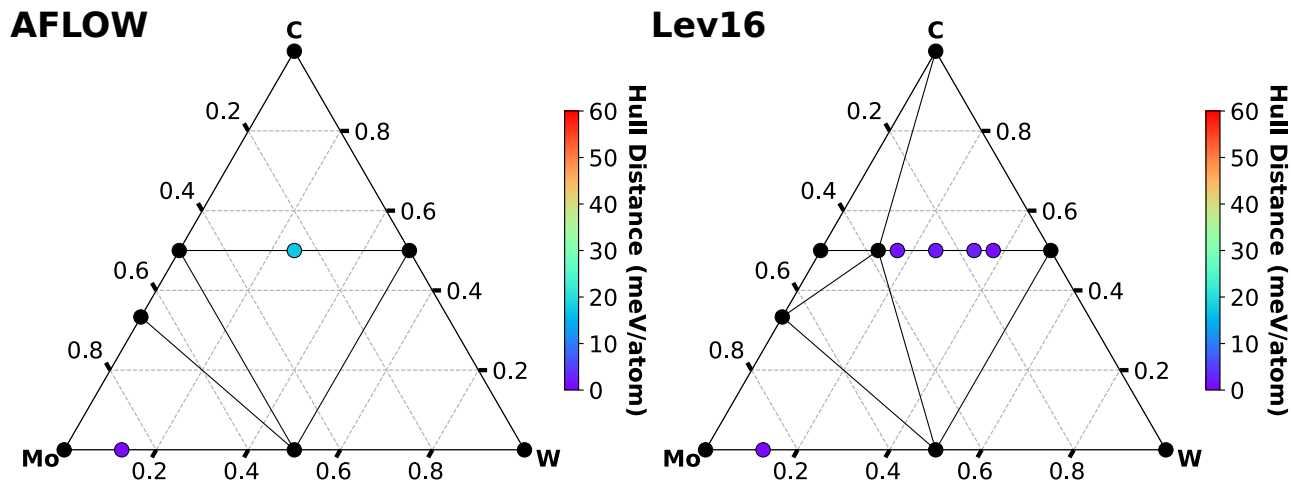


FIG. 3. Convex hulls obtained by DFT-optimizing structures predicted to be within 50 meV/atom of the convex hull obtained from AFLOW (left) and the PRAPs procedure at an MTP level of 16 (right) for the CMoW system. The black dots are structures lying on the convex hull, and phases within 60 meV/atom of the hull are represented by color dots (see color bar). Purple dots are within 1 meV/atom of the hull.

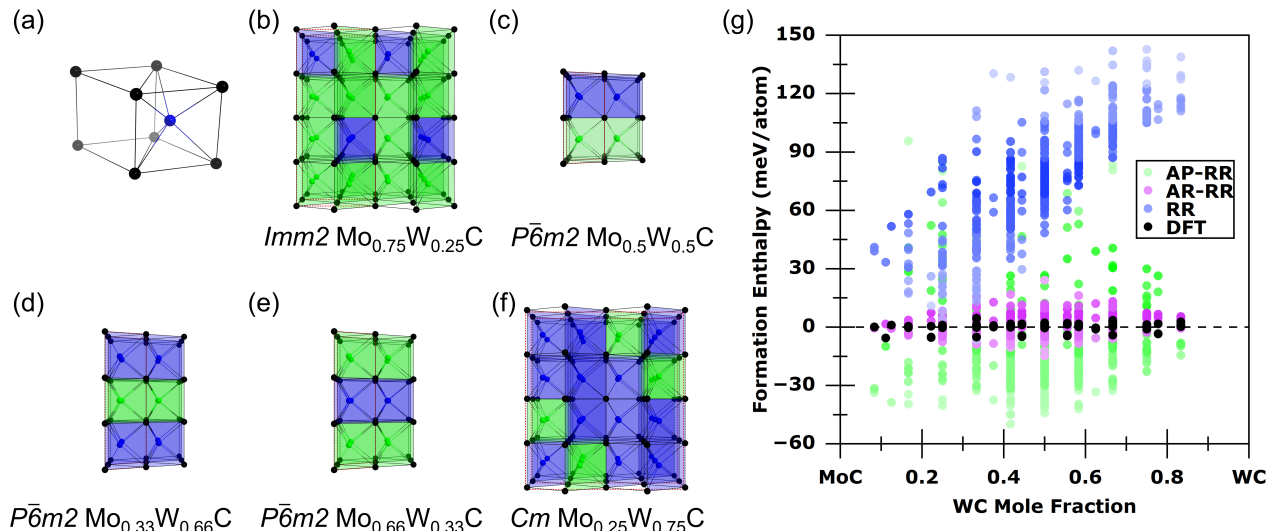


FIG. 4. Crystal structures of (a) parent phases:  $P\bar{6}m2$  WC (isostructural with MoC), (b)  $Imm2$   $Mo_{0.75}W_{0.25}C$ , (c)  $P\bar{6}m2$   $Mo_{0.5}W_{0.5}C$ , (d)  $P\bar{6}m2$   $Mo_{0.33}W_{0.66}C$ , (e)  $P\bar{6}m2$   $Mo_{0.66}W_{0.33}C$  and (f)  $Cm$   $Mo_{0.25}W_{0.75}C$ . Carbon atoms are colored black, tungsten atoms are blue and molybdenum atoms are green. Colored polyhedra are employed to emphasize the decoration of the structure by the two types of metal atoms. The  $c$ -axis is oriented perpendicular to the metal/carbon triangular nets. (g) The formation enthalpy,  $\Delta H$ , in meV/atom for the reaction  $(1-x)MoC + x(WC) \rightarrow Mo_{1-x}W_xC$  as a function of MoC/WC composition. DFT values (black dots) are provided along with results obtained following relaxation with the robust potential (RR), prediction of the energetics of the RR structures with the accurate potential (AP-RR), and further relaxation of the RR structures with the accurate potential (AR-RR) given by blue, green and pink dots, respectively.

same hexagonal prototype.

The identified near-and-on-hull phases lie on a straight line joining the two end-members comprising this CMo/CW series. They represent examples of an ensemble of phases with highly-variable concentrations, suggesting the existence of a solid solution with a very low critical temperature of the miscibility gap. To investigate this, we optimized  $\sim 366$   $Mo_{1-x}W_xC$  structures ( $x = 0.08\bar{3}, 0.1, 0.125, 0.16, 0.2, 0.25, 0.3, 0.375, 0.41\bar{6}, 0.4, 0.5, 0.5, 0.58\bar{3}, 0.625, 0.6, 0.75,$

$0.7, 0.8\bar{3}$ ) with 4-24 atoms in the unit cell, and between 2 and 86 unique structures were optimized per composition. The previously generated level 16 robust and accurate potentials were used to predict their energies and to relax them. Figure 4(g) plots the resulting enthalpies of formation,  $\Delta H$ , from the monocarbide endpoints: relaxed with the robust potential (RR), subsequently predicted by the accurate potential (AP-RR), and finally relaxed with the accurate potential (AR-RR).

All of the DFT-optimized compounds fell on or within



5.7 meV/atom of the line joining the CMo and CW end points, suggesting that their  $\Delta H$  is close to 0 meV/atom. For a given composition, various decorations were computed to be nearly isoenthalpic, suggesting that configurational entropy will play a role in the stability of this family of structures. Turning to the results obtained with the generated MTPs, the computed  $\Delta H$ , as predicted on structures relaxed by the RP, was largely positive (blue dots) with the deviation from the zero-energy line steadily increasing for larger W concentrations. Whereas the distance from the CMo-CW tie-line, averaged over all structures, was calculated as being 0.83 meV/atom ( $\sigma = 1.10$ ) via DFT, the robust relaxed protocol resulted in an average tie-line distance of 78.39 meV/atom ( $\sigma = 28.95$ ). Prediction of the energies of the robust relaxed structures with the AP (green dots) yielded an average  $\Delta H$  of 18.82 meV/atom ( $\sigma = 14.96$ ). It is only via relaxation with the AP (purple dots) that we obtain an average tie-line distance of 4.20 meV/atom ( $\sigma = 3.58$ ). This example illustrates that structural relaxation with the AP is key for obtaining energetics that are in good agreement with those derived from DFT calculations.

The convex hulls discussed and presented above (Figure 3) were optimized with DFT, and the conclusions regarding thermodynamic stability of particular phases were made based upon these hulls. This procedure is common-place [71] but it might make one wonder about the limits of the utility of ML-IAPs in CSP. Part of the answer lies above where we show that ML can significantly reduce the number of required DFT calculations. But, the other part of this answer is in the convex hull candidate structures: the output of PRAPs relaxations and predictions before the final DFT step. The analysis of the CMoW system suggested that relaxation with the AP is key for obtaining energetics that are in-line with DFT results. To further study this aspect, in Figure 5 we plot the convex hulls for the CHfTa system calculated at an MTP level of 22. Comparison of the AFLOW derived hull with one that is obtained after relaxation with the robust potential (RR) shows that the latter predicts a structure that is not found within AFLOW, with Hf<sub>0.5</sub>TaC<sub>0.5</sub> composition, to lie on the hull (after DFT relaxation, it falls 123 meV/atom above the hull) whereas Hf<sub>1-x</sub>Ta<sub>x</sub>C stoichiometries lie around 15 meV/atom above the hull. The rogue Hf<sub>0.5</sub>TaC<sub>0.5</sub> structure disappears after AP prediction, and the energies of the Hf<sub>1-x</sub>Ta<sub>x</sub>C species fall onto-and-just-above the hull. Relaxation with the AP yields a hull that is virtually indistinguishable from the one derived from AFLOW, similar to the results obtained for the CMoW system. In the Supplementary Information we provide these same four convex hulls for each carbide system considered and each MTP level, before and after subsequent relaxation with DFT. Generally speaking, the structures that fall within 60 meV/atom of the convex hull, after being relaxed with the RP followed by the AP, also fall within 60 meV/atom of to finish. These examples suggest that relaxations performed with an AP will be useful as a further screening step that can be undertaken prior to performing expensive DFT calculations in the materials prediction workflow.

## D. Discussion

The density functional theory (DFT) computed energies, forces and stresses found within the AFLOW database of four ternary carbide systems (HfTaC, HfZrC, MoWC and TaTiC) were employed to train system specific machine learning interatomic potentials of the moment tensor potential (MTP) flavor. A utility package that can be used to generate both robust potentials (RP), capable of roughly relaxing any structure, and accurate potentials (AP), tailored towards the relaxation of low-energy structures, which was employed to automate this training, is described. The AFLOW data was augmented with  $\sim 6300$  random symmetric structures resembling those that would be created in the first step of a crystal structure prediction (CSP) search, and these were relaxed with MTPs updated via active learning. For the HfTaC system, relaxation with the AP yielded a convex hull that agreed perfectly with the one found within AFLOW. Moreover, this procedure identified five Mo<sub>1-x</sub>W<sub>x</sub>C stoichiometry compounds, not found within AFLOW, that lay on the convex hull and corresponded to colorings of the hexagonal CMo/CW prototypes, illustrating how the described protocol can accelerate CSP. Subsequently, the RP and AP were used to relax hundreds of Mo<sub>1-x</sub>W<sub>x</sub>C lattices spanning a broad composition range, and it was shown that relaxation with the AP yielded formation enthalpies that were in excellent agreement with those computed via DFT, and the resulting convex hull exhibits regions in which entropy plays a considerable role on the phase stability. The ideas and tools described here may aid in the generation of ML-IAPs from already existing DFT data, to be used for materials prediction.

## METHODS

### E. Computational Details

The density functional theory (DFT) calculations were performed using the Vienna *ab initio* Simulation Package version 5.4.12 [72] coupled with the Perdew, Burke, Ernzerhof (PBE) gradient-corrected exchange and correlation functional [73] and the projector augmented wave method [74]. During the active learning procedure, the VASP calculations were performed using  $\Gamma$ -centered Monkhorst-Pack  $k$ -meshes where the number of divisions along each reciprocal lattice vector was chosen such that the product of this number with the real lattice constant was 30 Å. The carbon  $2s^2 2p^2$ , Hf  $6s^2 5d^2$ , Ta  $6s^2 5d^3$ , Zr  $5s^2 4d^2$ , Ti  $4s^1 3d^3$ , Mo  $5s^2 4d^4$  and W  $6s^2 5d^4$  electrons were treated as valence, and an energy cut-off of 400 eV was employed. After training was complete, the convex hull analysis included a DFT relaxation accomplished by calling AFLOW's management protocol, using the standard settings described in Ref.[57]; the AFLOW hull data was also re-relaxed using this procedure. Structures from the AFLOW database and those generated by RANDSPG [56], as described in the main text, comprised the full relaxation set employed for the development of the MTPs. The crystals whose geometries were relaxed to construct Figure 4 (g) were generated from  $P6m2$  Mo<sub>0.5</sub>W<sub>0.5</sub>C using the Supercell program, em-

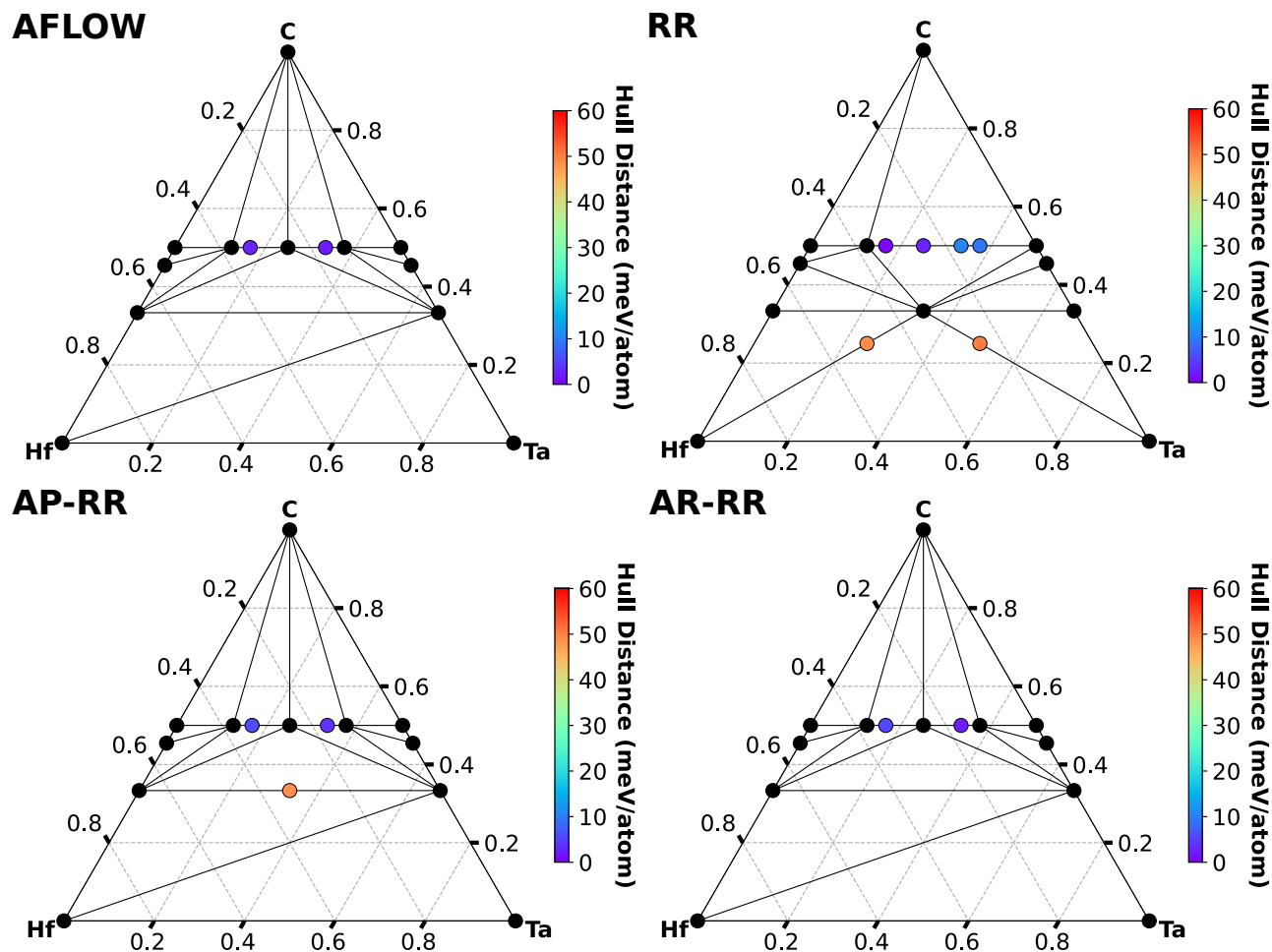


FIG. 5. Structures within 60 meV/atom of the AFLOW derived convex hull (top left), as well as the PRAPs procedure at an MTP level of 22 for the  $\text{CHfTa}$  system. Structures are colored (see color bar) according to the distances from the hull obtained after relaxing with the robust potential (RR), prediction of the enthalpies of the RR structures with the accurate potential (AP-RR) and relaxing structures with the accurate potential (AR-RR). Black dots are on the hull, and purple dots are within 1 meV/atom of the hull. In contrast to the plots shown in Figure 3, the data illustrated here has not undergone further DFT relaxations.

ploying the merge option to remove duplicate structures [75].

PRAPs was run on each ternary carbide using MTP levels 10, 16, and 22 with a MLIP-relaxation-iteration limit of 100, and an extrapolation grade of  $2 < \gamma \leq 10$ . The cutoff distances for generating the MTP were  $1.1 \text{ \AA} < x < 5 \text{ \AA}$ . Active learning was, in most cases, declared to be converged when no additional structures were considered for addition to the training set. In the case of the level 22 trainings, the ALS procedure was stopped when the number of structures to be added to the training set was less than 1% of the number already in the training set. PRAPs filtered out configurations with interatomic distances  $1.1 \text{ \AA} < d < 3.1 \text{ \AA}$  before beginning the pre-training, and when beginning the AP training removed all structures that were higher than 50 meV/atom of the most stable configuration for each composition.

**Code Availability.** The PRAPs code will be released in a subsequent publication, and in the meanwhile, may be obtained from the corresponding authors upon reasonable

request.

**Data Availability** The datasets generated during and/or analyzed during the current study are summarized in the supplementary information, and are available from the corresponding author on reasonable request.

**Acknowledgements** We would like to gratefully acknowledge the DoD SPICES MURI sponsored by the Office of Naval Research (Naval Research contract N00014-21-1-2515) for their financial support of this work. Calculations were performed at the Center for Computational Research at SUNY Buffalo (<http://hdl.handle.net/10477/79221>). We would like to acknowledge Xiaoyu Wang for artistic help and guidance, Masashi Kimura for assistance with the convex hull diagrams, Hagen Eckert, Xiomara Campilongo and Corey Oses for fruitful discussions.

**Author Contributions** E.Z. and S.C. conceived the research and supervised the study. J.R. carried out the method development of the PRAPs code, and performed the calculations and analysis. All authors participated in discussing the results, and commented on the manuscript.

### Additional Information

**Supplementary information** accompanies the paper on the *npj Computational Materials* website.










**Competing Interests:** The authors declare no competing interests.

- 
- [1] Liu, X., Zhang, J. & Pei, Z. Machine learning for high-entropy alloys: Progress, challenges and opportunities. *Prog. Mater. Sci.* **131**, 101018 (2023).
- [2] Zhang, L., Han, J., Wang, H., Car, R. & E, W. Deep potential molecular dynamics: A scalable model with the accuracy of quantum mechanics. *Phys. Rev. Lett.* **120**, 143001 (2018).
- [3] Grabowski, B. *et al.* Ab initio vibrational free energies including anharmonicity for multicomponent alloys. *npj Comput. Mater.* **5**, 80 (2019).
- [4] Tong, Q. *et al.* Combining machine learning potential and structure prediction for accelerated materials design and discovery. *J. Phys. Chem. Lett.* **11**, 8710–8720 (2020).
- [5] Falls, Z., Avery, P., Wang, X., Hilleke, K. P. & Zurek, E. The xtalopt evolutionary algorithm for crystal structure prediction. *J. Phys. Chem. C* **125**, 1601–1620 (2021).
- [6] Behler, J. & Parrinello, M. Generalized neural-network representation of high-dimensional potential-energy surfaces. *Phys. Rev. Lett.* **98**, 146401 (2007).
- [7] Hajinazar, S., Shao, J. & Kolmogorov, A. N. Stratified construction of neural network based interatomic models for multicomponent materials. *Phys. Rev. B* **95**, 014114 (2017).
- [8] Thompson, A. P., Swiler, L. P., Trott, C. R., Foiles, S. M. & Tucker, G. J. Spectral neighbor analysis method for automated generation of quantum-accurate interatomic potentials. *J. Comput. Phys.* **285**, 316–330 (2015).
- [9] Shapeev, A. V. Moment tensor potentials: A class of systematically improvable interatomic potentials. *Multiscale Model. Sim.* **14**, 1153–1173 (2016).
- [10] Bartók, A. P., Payne, M. C., Kondor, R. & Csányi, G. Gaussian approximation potentials: The accuracy of quantum mechanics, without the electrons. *Phys. Rev. Lett.* **104**, 136403 (2010).
- [11] Xie, S. R., Rupp, M. & Hennig, R. G. Ultra-fast interpretable machine-learning potentials. *npj Comp. Mat.* **9**, 162 (2023).
- [12] Pickard, C. J. Ephemeral data derived potentials for random structure search. *Phys. Rev. B* **106**, 014102 (2022).
- [13] Yang, Q. *et al.* Hard and superconducting cubic boron phase via swarm-intelligence structural prediction driven by a machine-learning potential. *Phys. Rev. B* **103**, 024505 (2021).
- [14] Podryabinkin, E. V., Tikhonov, E. V., Shapeev, A. V. & Oganov, A. R. Accelerating crystal structure prediction by machine-learning interatomic potentials with active learning. *Phys. Rev. B* **99**, 064114 (1–7) (2019).
- [15] Deringer, V. L., Pickard, C. J. & Csányi, G. Data-driven learning of total and local energies in elemental boron. *Phys. Rev. Lett.* **120**, 156001 (2018).
- [16] Deringer, V. L. & Csányi, G. Machine learning based interatomic potential for amorphous carbon. *Phys. Rev. B* **95**, 094203 (2017).
- [17] Deringer, V. L., Pickard, C. J. & Proserpio, D. M. Hierarchically structured allotropes of phosphorus from data-driven exploration. *Angew. Chem. Int. Ed.* **59**, 15880–15885 (2020).
- [18] Wang, X. *et al.* Data-driven prediction of complex crystal structures of dense lithium. *Nat. Commun.* **14**, 2924 (2023).
- [19] Ibarra-Hernandez, W. *et al.* Structural search for stable mg-ca alloys accelerated with a neural network interatomic model. *Phys. Chem. Chem. Phys.* **20**, 27545–27557 (2018).
- [20] Kharabadzze, S., Thorn, A., Koulakova, E. A. & Kolmogorov, A. N. Prediction of stable li-sn compounds: boosting ab initio searches with neural network potentials. *npj Comput. Mater.* **8**, 136 (2022).
- [21] Thorn, A., Gochitashvili, D., Kharabadzze, S. & Kolmogorov, A. N. Machine learning search for stable binary sn alloys with na, ca, cu, pd and ag. *Phys. Chem. Chem. Phys.* **25**, 22415–22436 (2023).
- [22] Wu, S. Q. *et al.* An adaptive genetic algorithm for crystal structure prediction. *J. Phys.: Condens. Matter* **26**, 035402 (2014).
- [23] Ferreira, P. P. *et al.* Search for ambient superconductivity in the lu-n-h system. *Nat. Commun.* **14**, 5367 (2023).
- [24] Salzbrenner, P. T. *et al.* Developments and further applications of ephemeral data derived potentials. *J. Chem. Phys.* **159**, 144801 (2023).
- [25] Gubaev, K., Podryabinkin, E. V., Hart, G. L. W. & Shapeev, A. V. Accelerating high-throughput searches for new alloys with active learning of interatomic potentials. *Comput. Mater. Sci.* **156**, 148–156 (2019).
- [26] Zuo, Y. *et al.* Performance and cost assessment of machine learning interatomic potentials. *J. Phys. Chem. A* **124**, 731–745 (2020).
- [27] Liu, Y. & Mo, Y. Assessing the accuracy of machine learning interatomic potentials in predicting the elemental orderings: A case study of li-al alloys. *Acta Materialia* **268**, 119742 (2024).
- [28] Bernstein, N., Csányi, G. & Deringer, V. L. De novo exploration and self-guided learning of potential-energy surfaces. *npj Comput. Mater.* **5**, 99 (2019).
- [29] Smith, J. S., Nebgen, B., Lubbers, N. & Isayev, O. Less is more: Sampling chemical space with active learning. *J. Chem. Phys.* **148**, 241733 (2018).
- [30] Zhang, L., Lin, D. Y., Wang, H., Car, R. & E, W. Active learning of uniformly accurate interatomic potentials for materials simulation. *Phys. Rev. Mater.* **3**, 023804 (2019).
- [31] Jinnouchi, R., Karsai, F. & Kresse, G. On-the-fly machine learning force field generation: Application to melting points. *Phys. Rev. B* **100**, 014105 (2019).
- [32] Curtarolo, S. *et al.* Aflow: An automatic framework for high-throughput materials discovery. *Comp. Mater. Sci.* **58**, 218–226 (2012).
- [33] Esters, M. *et al.* aflow.org: A web ecosystem of databases, software and tools. *Comput. Mater. Sci.* **216**, 111808 (2023).
- [34] Oses, C. *et al.* aflow++: A C++ framework for autonomous materials design. *Comput. Mater. Sci.* **217**, 111889 (2023).
- [35] Jain, A. *et al.* Commentary: The materials project: A materials genome approach to accelerating materials innovation. *APL Mater.* **1**, 011002 (2013).
- [36] Saal, J. E., Kirklin, S., Aykol, M., Meredig, B. & Wolverton, C. Materials design and discovery with high-throughput density functional theory: The open quantum materials database

- (oqmd). *JOM-J Min Met Mat S* **65**, 1501–1509 (2013).
- [37] Draxl, C. & Scheffler, M. The nomad laboratory: from data sharing to artificial intelligence. *J Phys-Mat.* **2**, 036001 (2019).
- [38] Ai, Q. *et al.* Ocelot: An infrastructure for data-driven research to discover and design crystalline organic semiconductors. *J Chem. Phys.* **154**, 174705 (2021).
- [39] NIST-Materials (2023). URL <https://materialsdata.nist.gov/>.
- [40] Chen, C. & Ong, S. P. A universal graph deep learning interatomic potential for the periodic table. *Nat. Comp. Sci.* **2**, 178–728 (2022).
- [41] Deng, B. *et al.* Chgnet as a pretrained universal neural network potential for charge-informed atomistic modelling. *Nat. Machine Intelligence* **5**, 1031–1041 (2023).
- [42] Choudhary, K. *et al.* Unified graph neural network force-field for the periodic table: solid state applications. *Digital Discovery* **2**, 346–355 (2023).
- [43] Batatia, I. *et al.* A foundation model for atomistic materials chemistry (2023). 2401.00096.
- [44] Merchant, A. *et al.* Scaling deep learning for materials discovery. *Nature* 1–6 (2023).
- [45] Novikov, I. S., Gubaev, K., Podryabinkin, E., V & Shapeev, A., V. The mlip package: moment tensor potentials with mpi and active learning. *Mach. Learn.: Sci. Technol.* **2**, 025002 (2021).
- [46] Schaarschmidt, M. *et al.* Learned force fields are ready for ground state catalyst discovery. *arXiv e-Prints* (2022). 2209.12466.
- [47] Hossain, M. D. *et al.* Entropy landscaping of high-entropy carbides. *Adv. Mater.* **33**, 2102904 (2021).
- [48] Hossain, M. D. *et al.* Carbon stoichiometry and mechanical properties of high entropy carbides. *Acta Mater.* **215**, 117051 (2021).
- [49] Nyshadham, C. *et al.* Machine-learned multi-system surrogate models for materials prediction. *npj Comput. Mater.* **5**, 75 (2019).
- [50] Jafary-Zadeh, M., Khoo, K. H., Laskowski, R., Branicio, P. S. & Shapeev, A., V. Applying a machine learning interatomic potential to unravel the effects of local lattice distortion on the elastic properties of multi-principal element alloys. *J Alloy. Compd.* **803**, 1054–1062 (2019).
- [51] Gubaev, K. *et al.* Performance of two complementary machine-learned potentials in modelling chemically complex systems. *npj Comput. Mater.* **9**, 129 (2023).
- [52] Zeng, C., Neils, A., Lesko, J. & Post, N. Machine learning accelerated discovery of corrosion-resistant high-entropy alloys. *Comput. Mater. Sci.* **237**, 112925 (2024).
- [53] Korotayev, P., Novoselov, I., Yanilkin, A. & Shapeev, A. Accessing thermal conductivity of complex compounds by machine learning interatomic potentials. *Phys. Rev. B* **100**, 144308 (2019).
- [54] Mortazavi, B. *et al.* Exploring phononic properties of two-dimensional materials using machine learning interatomic potentials. *Appl. Mater. Today* **20**, 100685 (2020).
- [55] Podryabinkin, E. V. & Shapeev, A. V. Active learning of linearly parametrized interatomic potentials. *Comp. Mater. Sci.* **140**, 171–180 (2017).
- [56] Avery, P. & Zurek, E. Randspg: An open-source program for generating atomistic crystal structures with specific space-groups. *Comput. Phys. Commun.* **213**, 208–216 (2017).
- [57] Calderon, C. E. *et al.* The aflow standard for high-throughput materials science calculations. *Comp. Mater. Sci.* **108**, 233–238 (2015).
- [58] Nakamura, K. & Yashima, M. Crystal structure of nacl-type transition metal monocarbides mc (m = v, ti, nb, ta, hf, zr), a neutron powder diffraction study. *Mater. Sci. Eng.-B Adv.* **148**, 69–72 (2008).
- [59] Clougherty, E. V., Kafalas, J. A. & Lothrop, K. H. A new phase formed by high-pressure treatment - face-centered cubic molybdenum monocarbide. *Nature* **191**, 1194 (1961).
- [60] Schuster, J., Rudy, E. & Nowotny, H. Moc-phase with wc structure. *Monatsh. Chem.* **107**, 1167–1176 (1976).
- [61] Harrington, T. J. *et al.* Phase stability and mechanical properties of novel high entropy transition metal carbides. *Acta Mater.* **166**, 271–280 (2019).
- [62] Vorotilo, S. *et al.* Phase stability and mechanical properties of carbide solid solutions with 2-5 principal metals. *Comp. Mater. Sci.* **201**, 110869 (2022).
- [63] Sarker, P. *et al.* High-entropy high-hardness metal carbides discovered by entropy descriptors. *Nat. Commun.* **9**, 4980 (2018).
- [64] Divilov, S. *et al.* Disordered enthalpy-entropy descriptor for high-entropy ceramics discovery. *Nature* 66–73 (2024).
- [65] Dai, F.-Z., Wen, B., Sun, Y., Xiang, H. & Zhou, Y. Theoretical prediction on thermal and mechanical properties of high entropy (zr0. 2hf0. 2ti0. 2nb0. 2ta0. 2) c by deep learning potential. *J Mater. Sci. Technol.* **43**, 168–174 (2020).
- [66] Pak, A. Y. *et al.* Machine learning-driven synthesis of tizrnbhf-tac5 high-entropy carbide. *npj Comput. Mater.* **9**, 7 (2023).
- [67] Mehl, M. J. *et al.* The aflow library of crystallographic prototypes: part 1. *Comp. Mater. Sci.* **136**, S1–S828 (2017).
- [68] Hicks, D. *et al.* The aflow library of crystallographic prototypes: part 2. *Comp. Mater. Sci.* **161**, S1–S1011 (2019).
- [69] Hicks, D. *et al.* The aflow library of crystallographic prototypes: part 3. *Comp. Mater. Sci.* **199**, 110450 (2021).
- [70] Hicks, D. *et al.* Aflow-xtalfinder: a reliable choice to identify crystalline prototypes. *npj Comput. Mater.* **7**, 30 (2021).
- [71] Roberts, J., Bursten, J. R. & Risko, C. Genetic algorithms and machine learning for predicting surface composition, structure, and chemistry: a historical perspective and assessment. *Chem. Mater.* **33**, 6589–6615 (2021).
- [72] Kresse, G. & Hafner, J. *Ab Initio* molecular dynamics for liquid metals. *Phys. Rev. B.* **47**, 558 (1993).
- [73] Perdew, J. P., Burke, K. & Ernzerhof, M. Generalized gradient approximation made simple. *Phys. Rev. Lett.* **77**, 3865–3868 (1996).
- [74] Blöchl, P. E. Projector augmented-wave method. *Phys. Rev. B* **50**, 17953 (1994).
- [75] Okhotnikov, K., Charpentier, T. & Cadars, S. Supercell program: a combinatorial structure-generation approach for the local-level modeling of atomic substitutions and partial occupancies in crystals. *J. Cheminformatics* **8**, 1–15 (2016).



# Machine Learned Interatomic Potentials for Ternary Carbides trained on the AFLOW Database

Josiah Roberts ,<sup>†</sup> Biswas Rijal ,<sup>†</sup> Simon Divilov ,<sup>‡</sup> Jon-Paul Maria ,<sup>§</sup>  
William G. Fahrenholtz ,<sup>||</sup> Douglas E. Wolfe ,<sup>§</sup> Donald W. Brenner ,<sup>⊥</sup>  
Stefano Curtarolo ,<sup>‡</sup> and Eva Zurek, <sup>\*,†</sup>

<sup>†</sup>*Department of Chemistry, State University of New York at Buffalo, Buffalo, NY 14260, USA*

<sup>‡</sup>*Department of Mechanical Engineering and Materials Science, Duke University, Durham, NC 27708, USA*

<sup>¶</sup>*Center for Autonomous Materials Design, Duke University, Durham, NC 27708, USA*

<sup>§</sup>*Department of Materials Science and Engineering, The Pennsylvania State University, University Park, PA 16802, USA*

<sup>||</sup>*Department of Materials Science and Engineering, Missouri University of Science and Technology, Rolla, MO 65409, USA*

<sup>⊥</sup>*Department of Materials Science and Engineering, North Carolina State University, Raleigh, NC 27695, USA*

E-mail: ezurek@buffalo.edu

## Contents

<b>S1 Plan for Robust and Accurate Potentials (PRAPs) Training</b>	<b>S2</b>
<b>S2 Training Data and Root Mean Square Errors</b>	<b>S2</b>
<b>S3 Convex Hulls</b>	<b>S7</b>

# S1 Plan for Robust and Accurate Potentials (PRAPs) Training

Table S1: The number of low energy configurations correctly and incorrectly predicted (A-B) and the number of high energy configurations correctly and incorrectly predicted (C-D) by PRAPs (denoted as A-B/C-D) for the ternary carbide systems studied at different MTP levels of theory. The Pre-Robust Potential (Pre-RP) and the Robust Potential (RP) are compared against the original AFLOW data (after removing structures with unphysically short interatomic distances). The Accurate Potential (AP) is used to make two predictions and two comparisons. First it is compared against the low-energy robust-relaxed data (AP-RR), and then compared against the low-energy AFLOW data (AP-Low).

Level 10	Pre-RP	RP	AP-RR	AP-Low
CHfTa	6-0/7-0	6-0/9-0	6-0/8-0	6-0/10-0
CHfZr	3-3/7-0	2-0/9-0	2-0/9-0	2-0/9-0
CMoW	8-0/8-0	6-0/9-0	3-0/10-0	6-0/3-1
CTaTi	7-0/7-0	4-0/4-0	4-0/8-0	4-0/7-0
Level 16	Pre-RP	RP	AP-RR	AP-Low
CHfTa	6-0/8-0	6-0/10-0	6-0/8-0	6-0/10-0
CHfZr	3-2/7-0	6-0/10-0	2-0/9-0	6-0/9-0
CMoW	8-0/4-0	7-0/10-0	7-0/8-0	7-0/1-1
CTaTi	8-0/6-0	7-0/4-0	6-0/9-0	7-0/8-0
Level 22	Pre-RP	RP	AP-RR	AP-Low
CHfTa	3-2/6-0	3-0/9-0	6-0/10-0	3-0/10-0
CHfZr	1-2/6-0	2-0/9-0	2-0/7-0	2-0/9-0
CTaTi	3-3/6-0	4-0/7-0	5-0/9-0	4-0/9-0

# S2 Training Data and Root Mean Square Errors

To better understand the factors contributing to the root mean square errors (RMSE), we plotted the DFT energies of the structures present in the AFLOW training set versus an arbitrarily chosen structure index in Figure S1. Configurations with interatomic distances outside of the range  $1.1 \text{ \AA} < x < 3.1 \text{ \AA}$ , were automatically filtered from the training set. While a majority of the configurations present possessed energies that fell within  $-9.5 \pm 1.0 \text{ eV/atom}$ , 5.6% fell outside this range, some by up to -40 meV/atom, and 30% fell outside of one standard deviation from the mean.

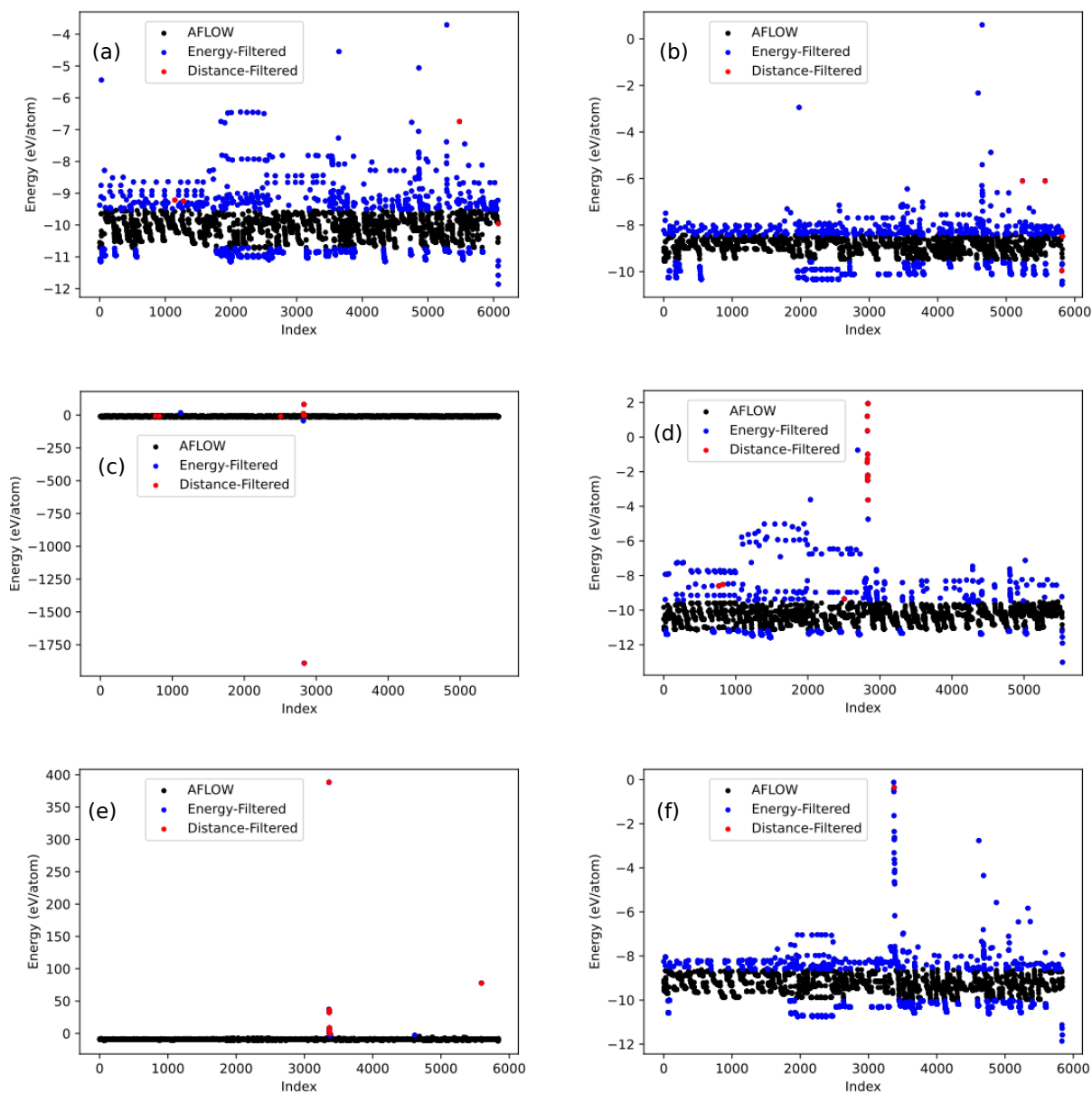


Figure S1: Energy values found in the original AFLOW data for: (a) CHfTa, (b) CHfZr, (c and d) CMoW raw and zoomed-in, and (e and f) CTaTi raw and zoomed-in. Configurations not removed by filtering are marked in black. Configurations removed by the distance filtering are marked in red. Configurations removed during testing of energy filtering are marked in blue.

PRAPs always filters structures by distance, but we considered the possibility of adding energy as a secondary filtering condition. After filtering by distance the remaining filtrate was filtered by only including configurations with energies within one standard deviation from the mean. A new robust potential (Level 10e) was generated from this filtered data and plots were generated to investigate the effect of the filtering on the energy predictions, appearing below in Figure S2.

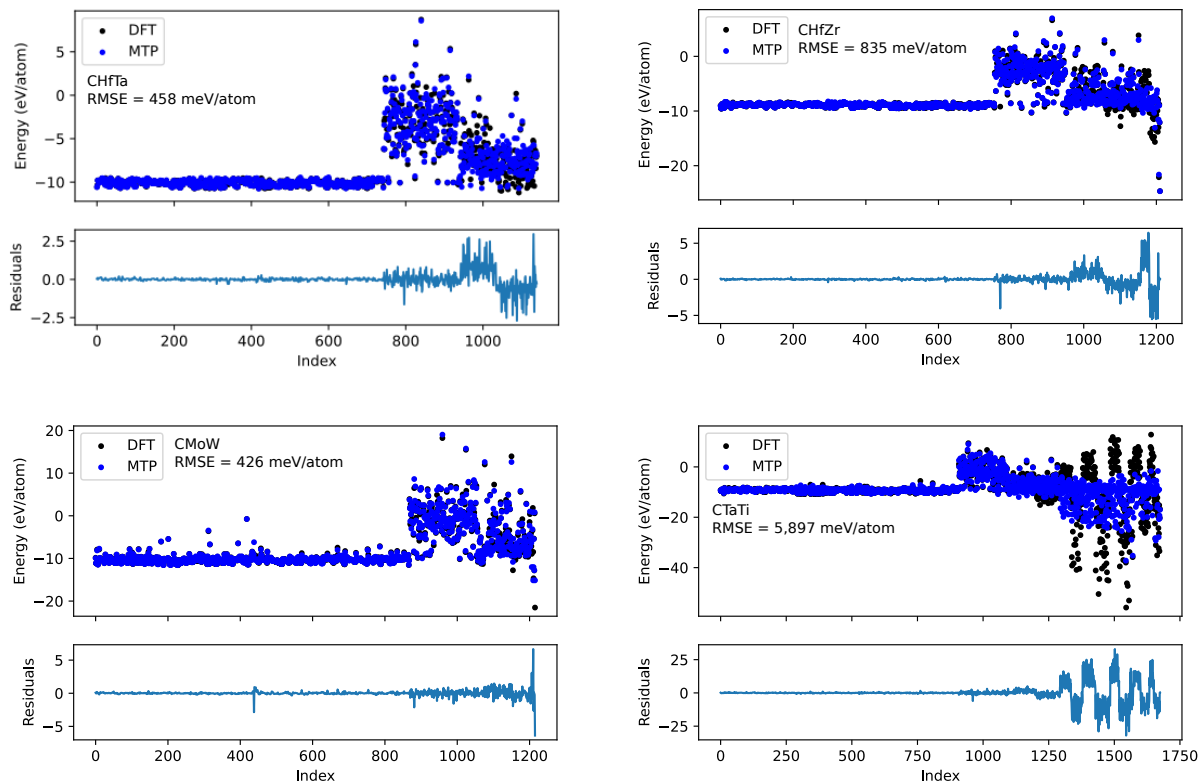


Figure S2: The AFLOW data (Figure S1, all dots) was filtered by both distance and energy (Figure S1, black dots) and submitted for training. Here we show the energies of the Robust Potential training set, as calculated by DFT and the Robust Potential (MTP, Level 10e). The training set contains two regions: the relatively flat region in the first half of the x-axis contains configurations straight from the AFLOW data found in Figure S1, the other region in the second half of the x-axis with the widely spread data contains configurations generated during the active learning procedure, which may include configurations that are not chemically sensible or converged, reflecting the quality of the generating MTP. The associated root-mean-square-errors appear in each plot (compare to 197, 302, 448, and 704 meV/atom, respectively, from the main text, Table II) and the differences between the DFT and Robust Potential appear below as residual traces.



To gain a better understanding of the predictive power of our MTPs and the origin of the previously-stated RMSEs, we examined the differences between the original AFLOW data and the trained potential’s prediction. In Table S2, we counted how many configurations had differences within one standard deviation of the mean and how many configurations had differences less-than 0.5 eV/atom. This was done for each system, for both Robust and Accurate Potentials, using the standard Level 10 data (see main text) and the energy-filtered data from above (Level 10e).

Table S2: Percent of the training set configurations whose predicted energies differed by less-than one standard deviation of the mean and less-than 0.5 eV/atom from the original AFLOW data.

Level 10	RP		AP	
	Stdev	< 0.5	Stdev	< 0.5
CHfTa	77.9%	84.3%	87.4%	99.6%
CHfZr	81.6%	80.5%	90.9%	99.3%
CMoW	81.3%	79.1%	86.4%	98.9%
CTaTi	85.7%	81.1%	87.3%	99.7%
Level 10e	RP		AP	
	Stdev	< 0.5	Stdev	< 0.5
CHfTa	77.2%	75.3%	87.0%	98.7%
CHfZr	79.2%	73.4%	89.9%	99.9%
CMoW	79.7%	78.5%	91.2%	97.7%
CTaTi	78.3%	55.4%	92.2%	72.4%

We performed a set of tests on each of the four systems at level 10 to test the effects of structural diversity. In these, we replaced the set of 6000 RandSPG structures of diverse space groups, with a set of 200 HCP, FCC, and BCC structures from RandSPG. The energy RMS values are reported in meV/atom in Table S3 with the original values from Table II of the main text in parentheses for comparison.

Table S3: Root mean square errors of the energy for training and prediction across the four systems where the lattices of the RandSPG structures were restricted to HCP, FCC, and BCC only. Original values from Table II of the main text are in parentheses.

System	Training Errors (meV/atom)			Prediction Errors (meV/atom)	
	Pre-trained	RP	AP	RP	AP
CHfTa	38 (34)	186 (197)	162 (179)	77 (77)	53 (70)
CHfZr	32 (31)	244 (302)	95 (136)	76 (92)	42 (89)
CMoW	66 (69)	458 (448)	152 (187)	489 (490)	80 (142)
CTaTi	43 (41)	803 (704)	279 (167)	251 (237)	150 (90)

Finally, we performed a small test at level 10 across all four systems to examine the usefulness of the pre-training procedure. The entire PRAPs training procedure was conducted, omitting the pre-training step, and the timings and errors were compared with those obtained from the original tests as described in the main text. The final DFT calculations and convex hull analysis were omitted as that time can be separated from the training time. The results are provided in Table S4. Omitting the pre-training gave significant improvements in speed at the cost of MTP quality, as measured by energy RMS error (values in parentheses are from the original run, Table II in the main text). Wall times (D-HH:MM:SS) were provided instead of CPU times for a more faithful estimate of run time.

Table S4: Comparison of PRAPs performance with and without the pre-training step. Times are given as Days-Hours:Minutes:Seconds. Error values are reported in meV/atom. The parentheses contain the errors for the control group at Level 10 with pre-training as reported in the main text, Table II.

System	Wall Time		Training Errors (meV/atom)		Prediction Errors (meV/atom)	
	Original	No Pre-train	RP	AP	RP	AP
CHfTa	7-20:50:57	6-00:08:55	622 (197)	109 (179)	183 (77)	105 (70)
CHfZr	8-10:27:47	8-02:14:44	613 (302)	94 (136)	160 (92)	136 (89)
CMoW	7-12:24:07	4-21:53:13	760 (448)	201 (187)	504 (490)	434 (142)
CTaTi	12-05:49:09	6-02:22:11	1104 (704)	296 (167)	329 (237)	188 (90)

## S3 Convex Hulls

This section contains a subset of the convex hulls calculated by PRAPs. If desired by the user, PRAPs will calculate eleven convex hulls: two for the DFT data before-and-after relaxation, and nine using the Robust and Accurate Potentials. Six of the hulls are presented here in a table-like format, organized into rows and columns from Figures S3 to S13. The AFLOW data (top row) is combined with the RANDSPG data and filtered to remove unphysical structures as described in the main text. This filtered set is then relaxed using the Robust Potential to form the Robust-Relaxed set (RR, second row). Then the RR set is filtered to obtain only configurations within 50 meV/atom of the lowest energy configuration for each composition and the Accurate Potential is used to relax these structures (AP-RR, bottom row). The Accurate Potential is also used on the AFLOW data to determine if it can reproduce the AFLOW convex hull (AP-v, not shown). The left column contains hulls generated from the MLIP output while the right shows the hulls of the same data after DFT relaxation via AFLOW’s standard procedure. To calculate the remaining hulls, PRAPs will concatenate two files together: the Post-Relaxation AFLOW convex hull (shown below in the top-right of each figure) and the Post-Relaxation Accurate Potential hulls (shown below in the middle-right and lower-right of each figure). This allows a direct comparison of the “literature” and “experiment” and will tell the user whether or not structures predicted by PRAPs are still on the convex hull when considering the original AFLOW data. These hulls are not shown below as almost all of the hulls remain unchanged from those already shown.

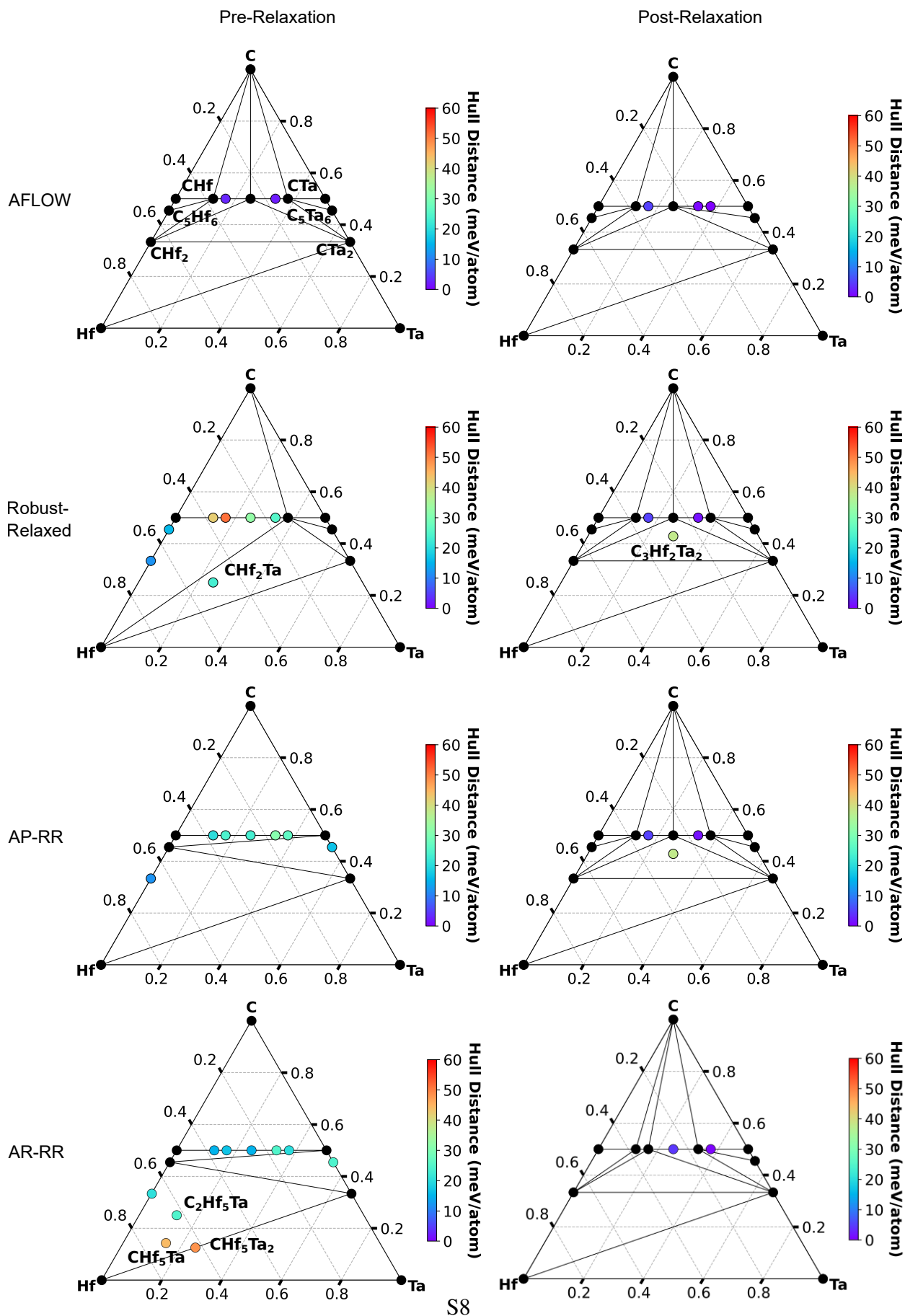


Figure S3: Convex Hulls of CHfTa at Level 10. The unlabeled structures on the line between CHf and CTa are, from left-to-right, C<sub>4</sub>Hf<sub>3</sub>Ta, C<sub>3</sub>Hf<sub>2</sub>Ta, C<sub>2</sub>HfTa, C<sub>3</sub>HfTa<sub>2</sub>, and C<sub>4</sub>HfTa<sub>3</sub>.



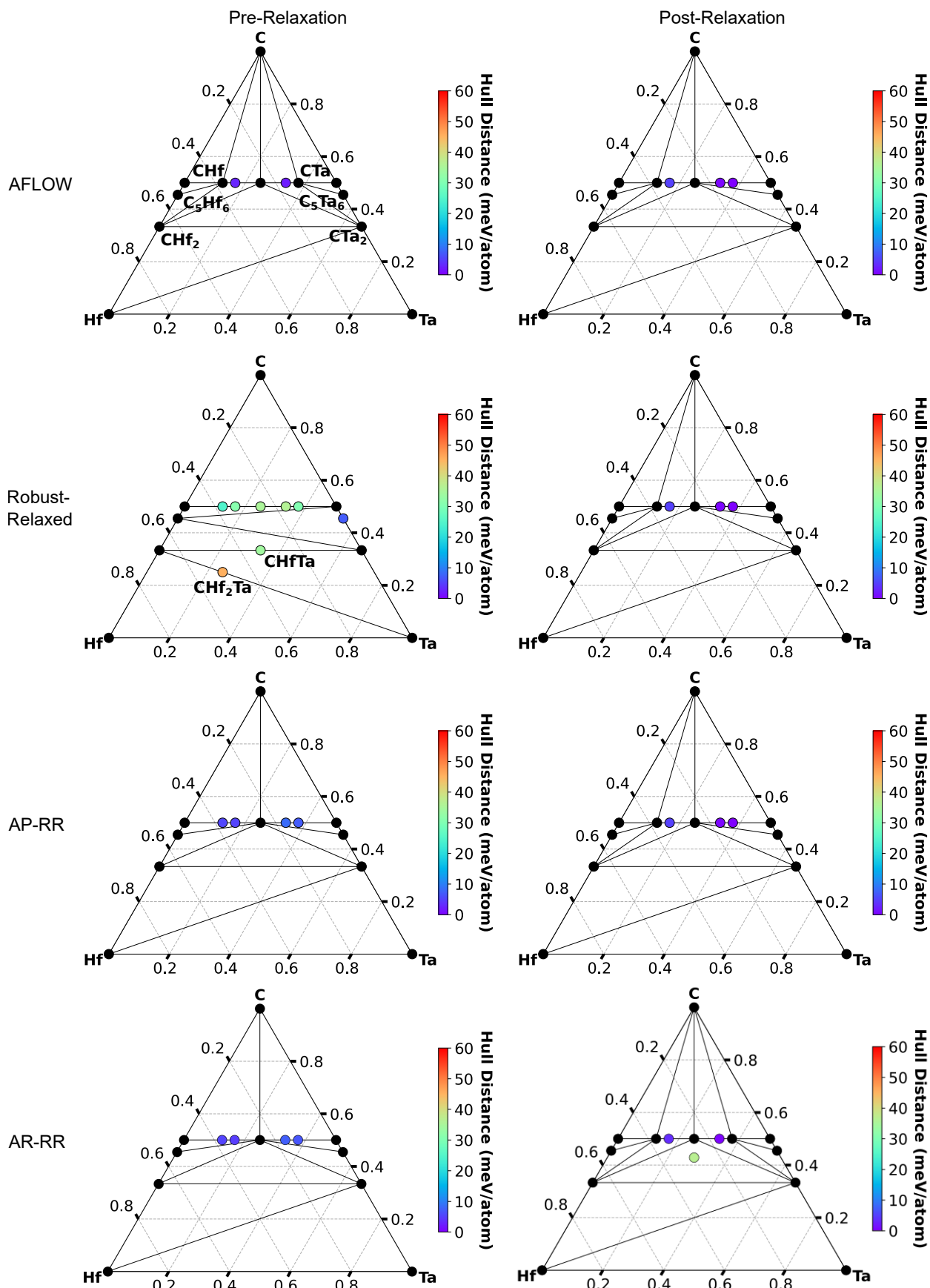


Figure S4: Convex Hulls of  $\text{CHfTa}$  at Level 16. The unlabeled structures on the line between  $\text{CHf}$  and  $\text{CTa}$  are, from left-to-right,  $\text{C}_4\text{Hf}_3\text{Ta}$ ,  $\text{C}_3\text{Hf}_2\text{Ta}$ ,  $\text{C}_2\text{HfTa}$ ,  $\text{C}_3\text{HfTa}_2$ , and  $\text{C}_4\text{HfTa}_3$ .

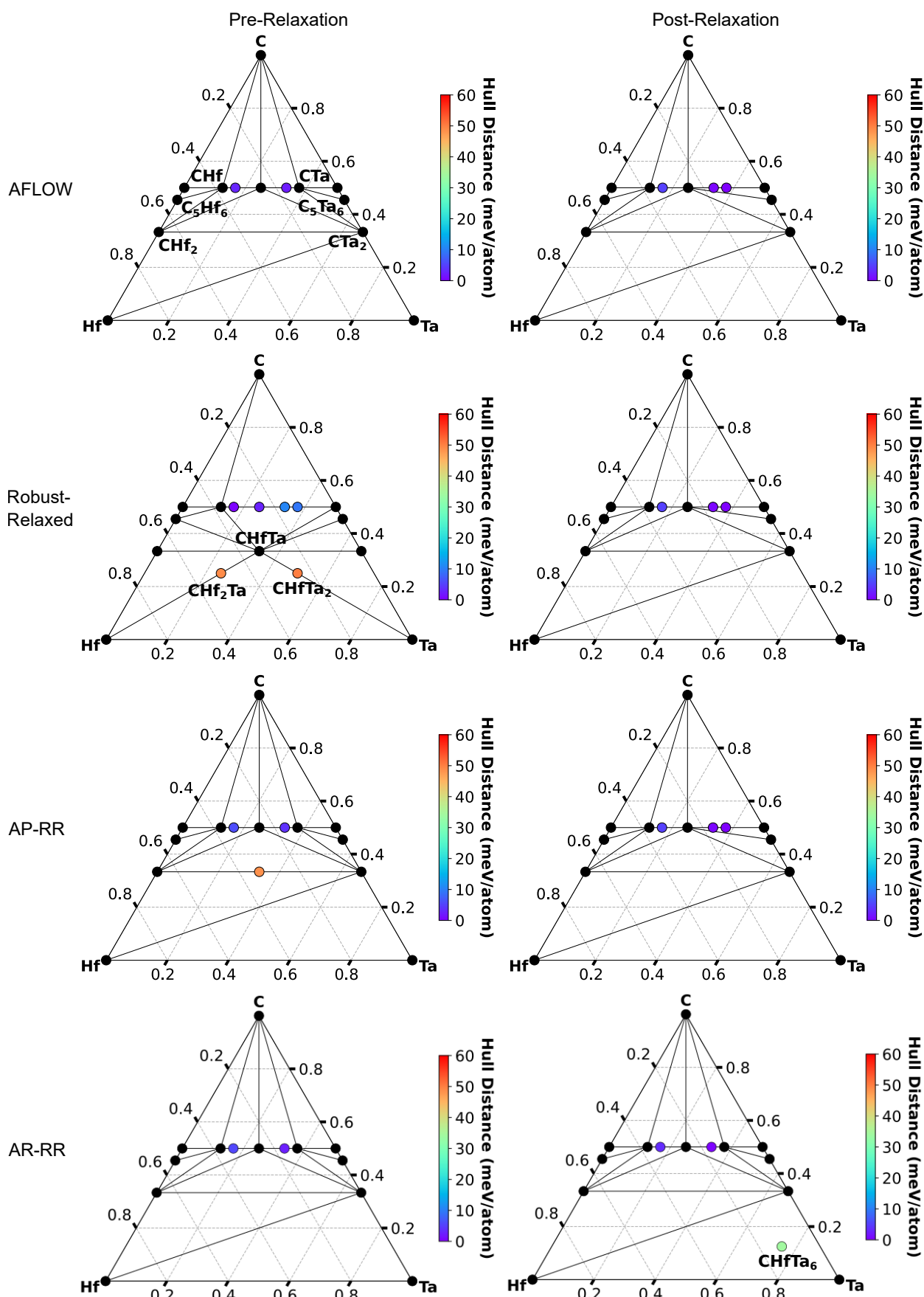
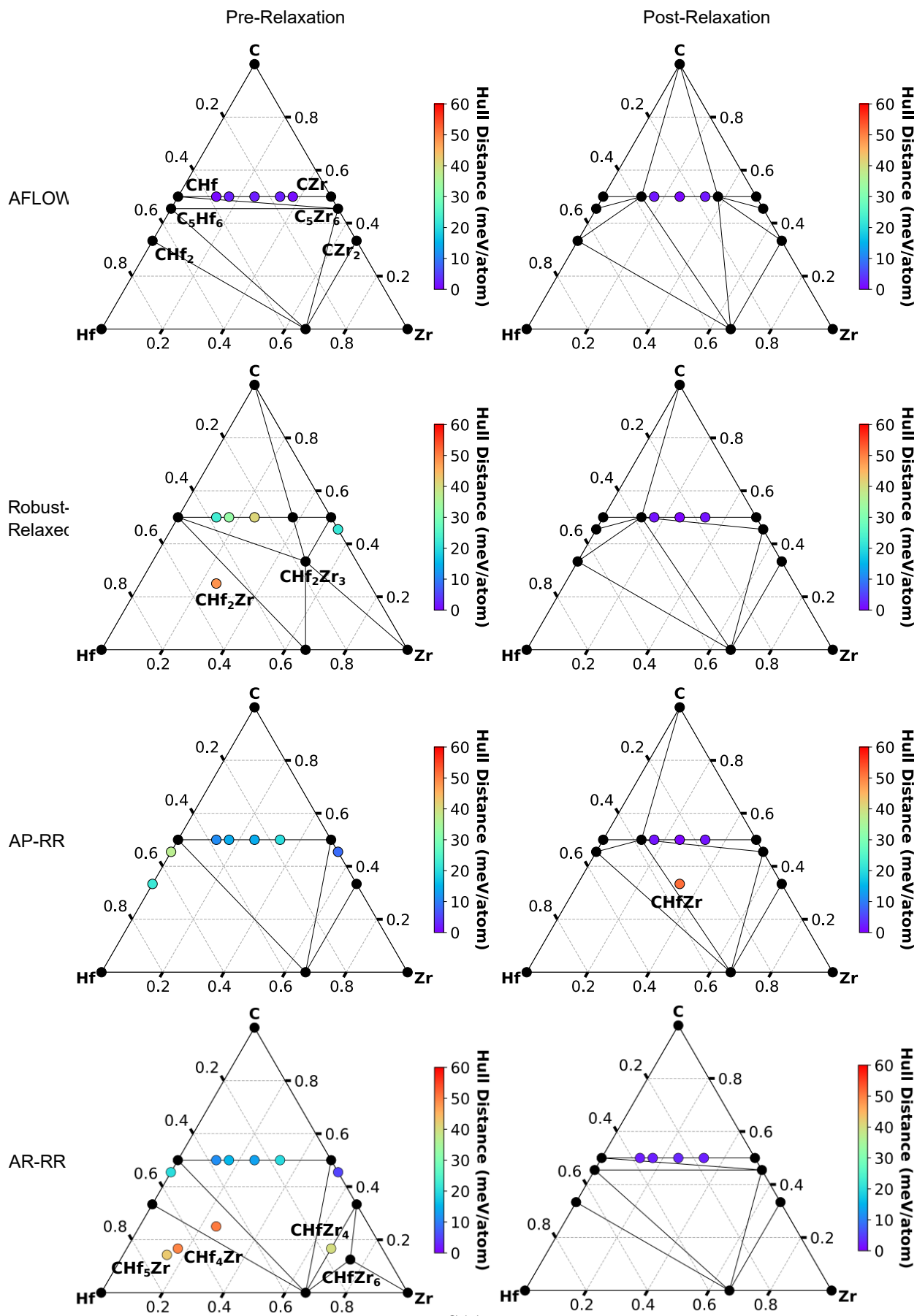


Figure S5: Convex Hulls of CHfTa at Level 22. The unlabeled structures on the line between CHf and CTa are, from left-to-right,  $C_4Hf_3Ta$ ,  $C_3Hf_2Ta$ ,  $C_2HfTa$ ,  $C_3HfTa_2$ , and  $C_4HfTa_3$ .



S11

Figure S6: Convex Hulls of CHfZr at Level 10. The unlabeled structures on the line between CHf and CZr are, from left-to-right, C<sub>4</sub>Hf<sub>3</sub>Zr, C<sub>3</sub>Hf<sub>2</sub>Zr, C<sub>2</sub>HfZr, C<sub>3</sub>HfZr<sub>2</sub>, and C<sub>4</sub>HfZr<sub>3</sub>.

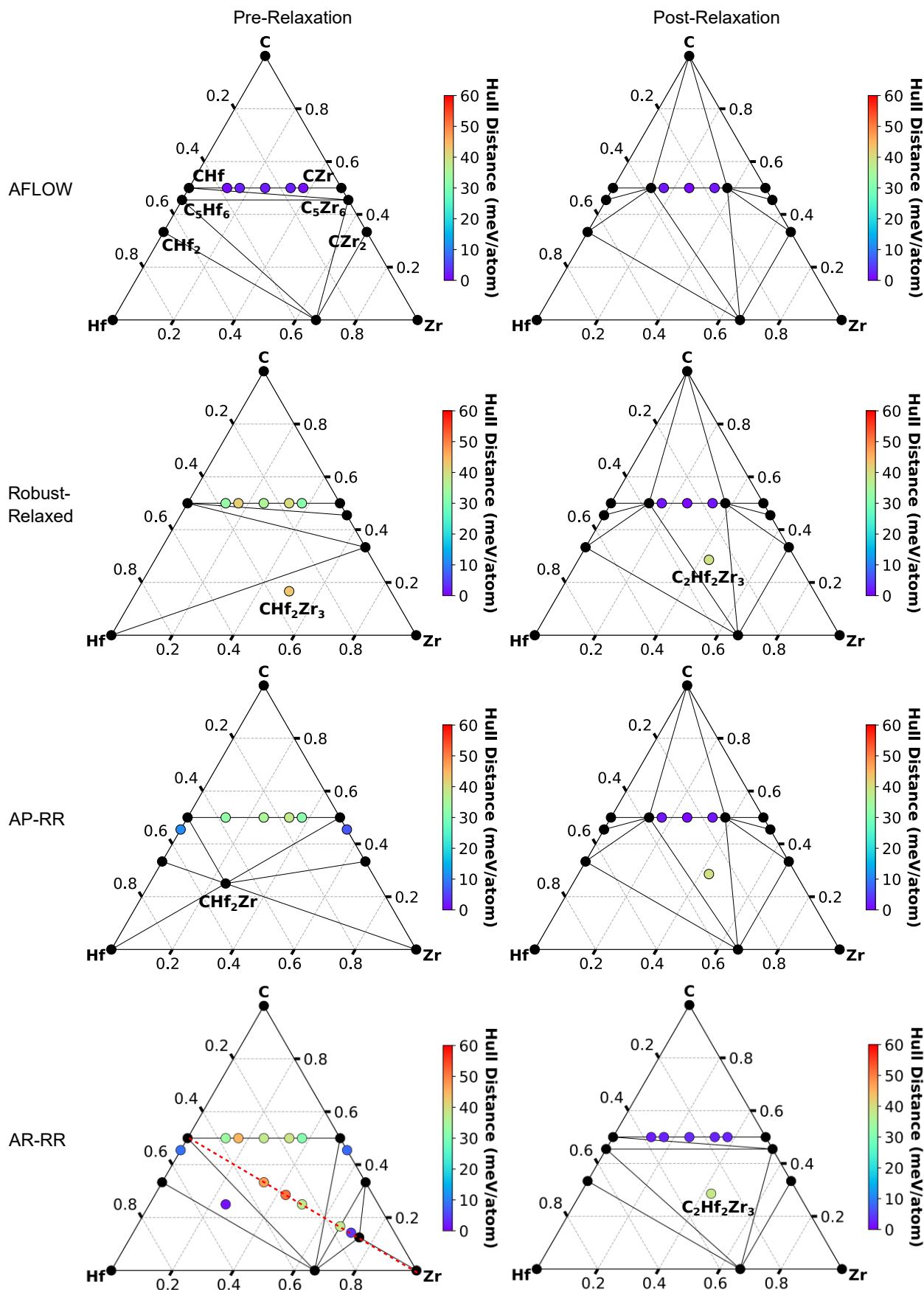


Figure S7: Convex Hulls of CHfZr at Level 16. The unlabeled structures on the line between CHf and CZr are, from left-to-right, C<sub>4</sub>Hf<sub>3</sub>Zr, C<sub>3</sub>Hf<sub>2</sub>Zr, C<sub>2</sub>HfZr, C<sub>3</sub>HfZr<sub>2</sub>, and C<sub>4</sub>HfZr<sub>3</sub>.

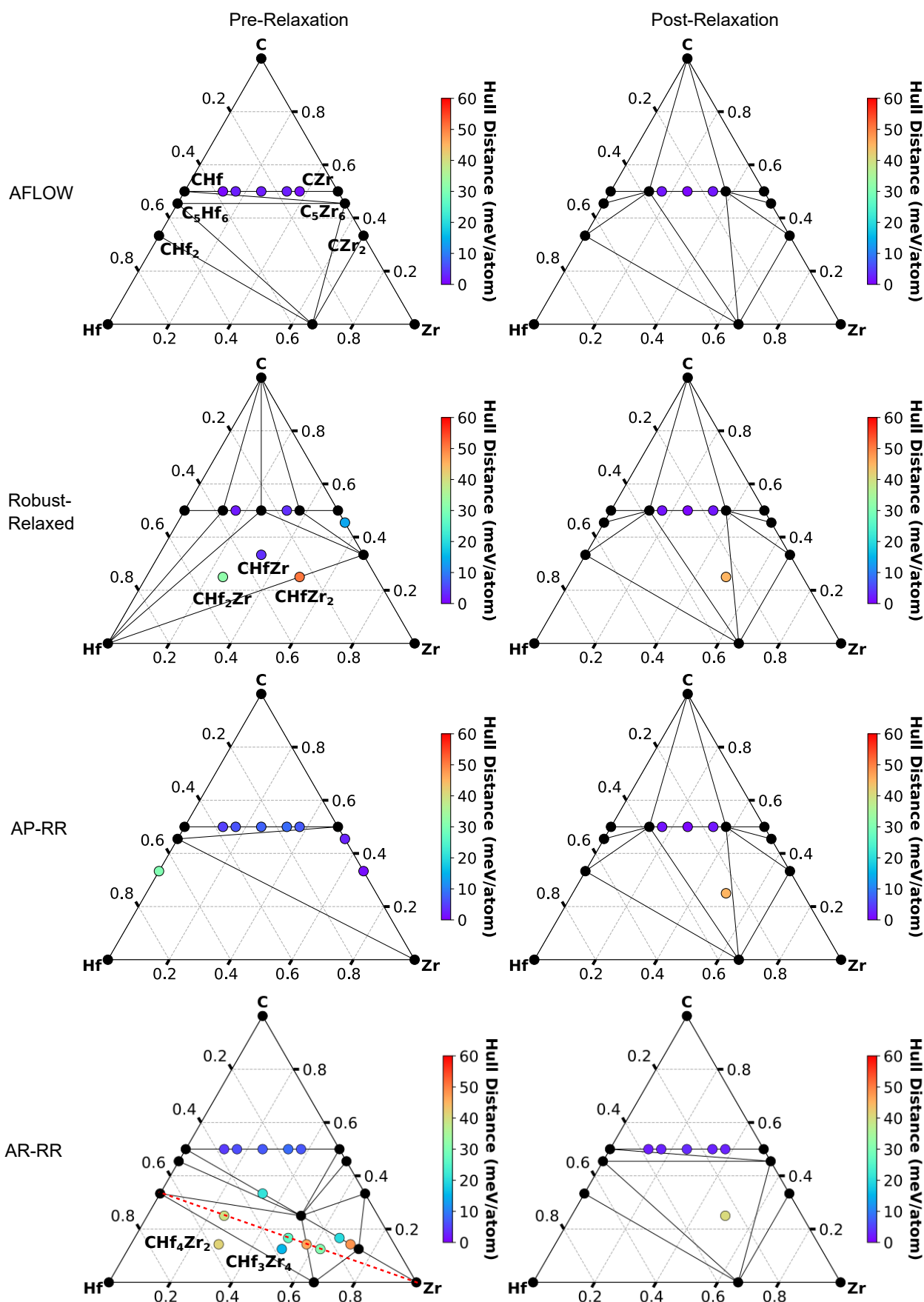


Figure S8: Convex Hulls of CHfZr at Level 22. The unlabeled structures on the line between CHf and CZr are, from left-to-right,  $C_4Hf_3Zr$ ,  $C_3Hf_2Zr$ ,  $C_2HfZr$ ,  $C_3HfZr_2$ , and  $C_4HfZr_3$ .

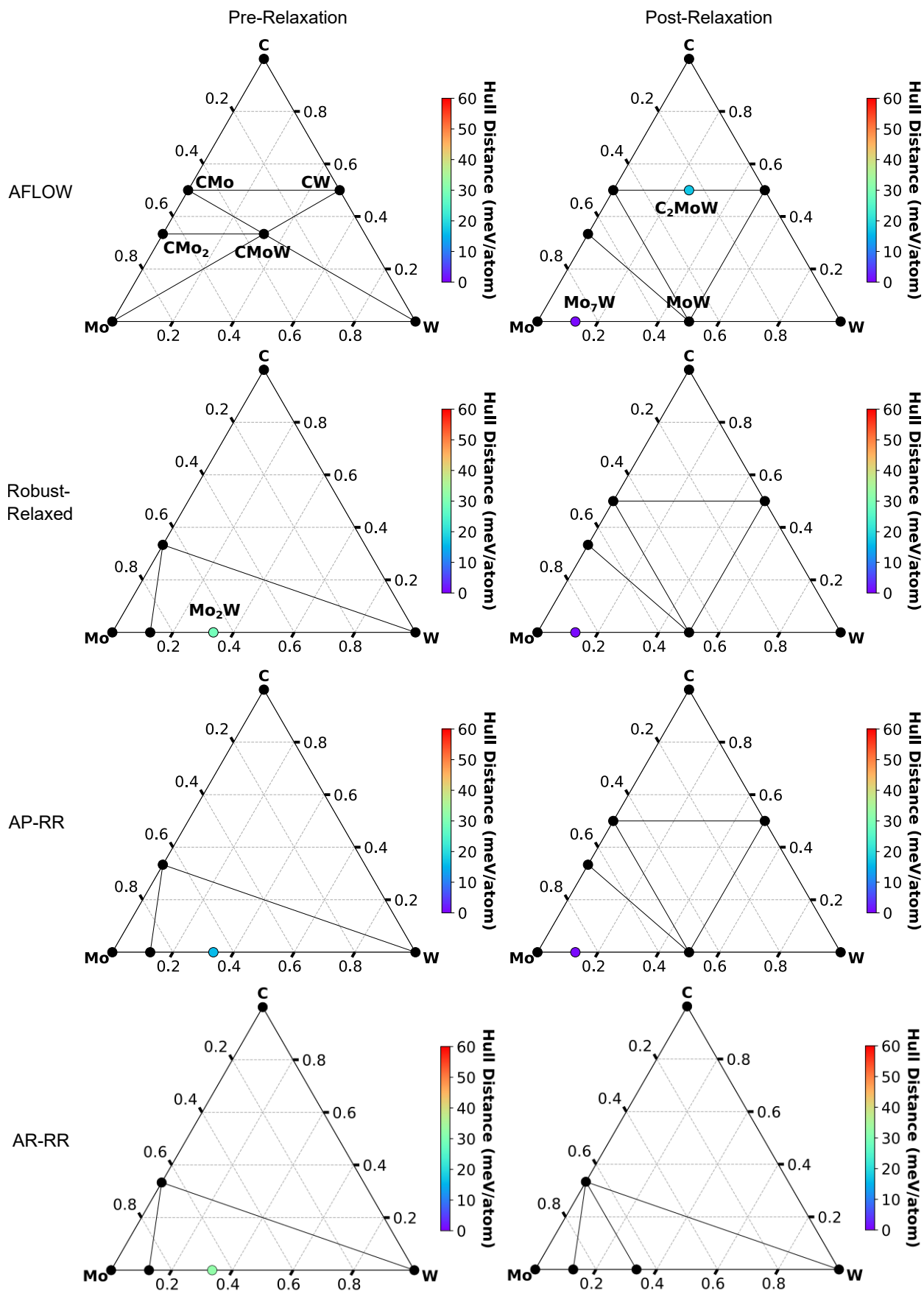


Figure S9: Convex Hulls of CMoW at Level 10.



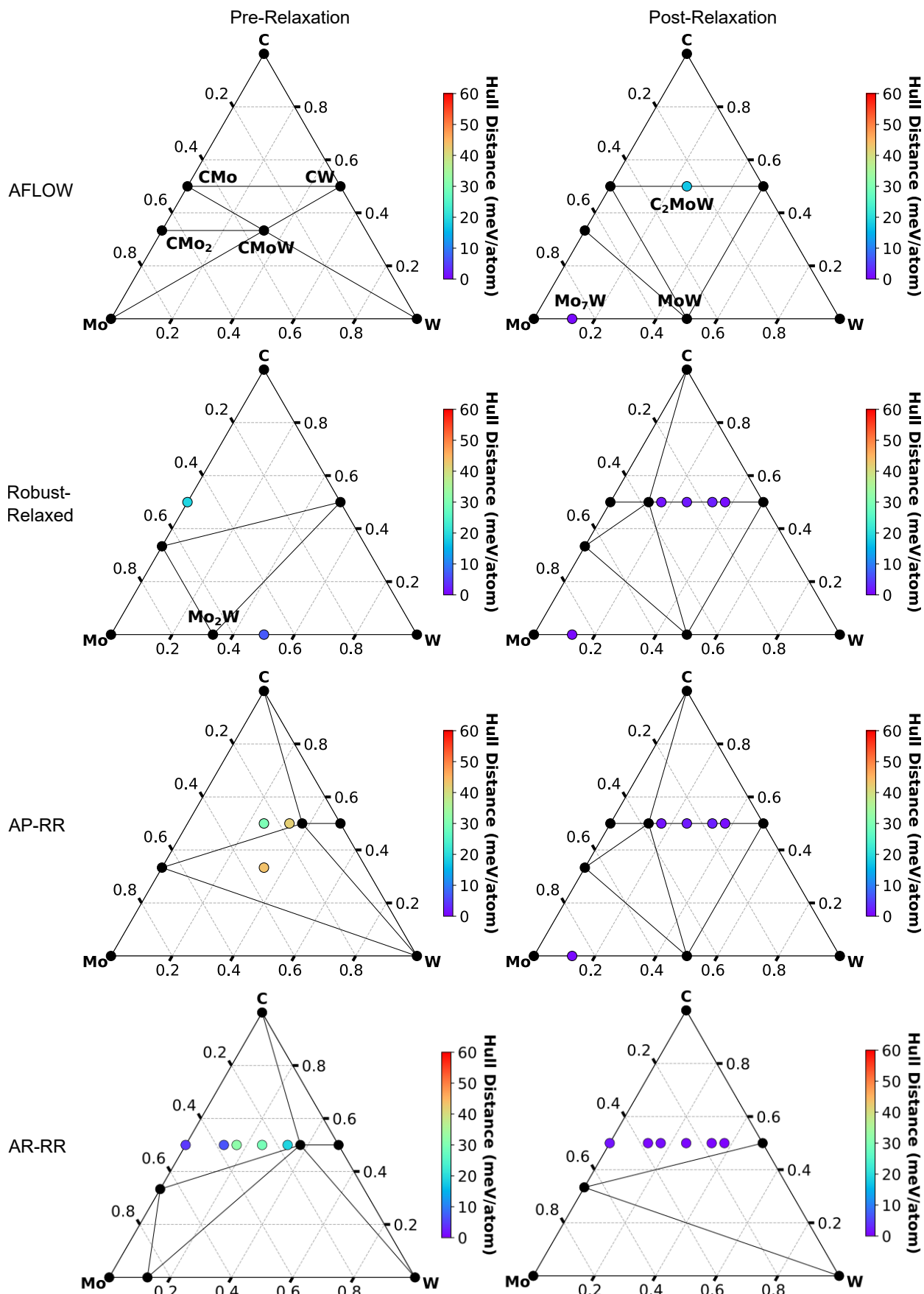


Figure S10: Convex Hulls of CMoW at Level S16. The unlabeled structures on the line between CMo and CW are, from left-to-right,  $C_4Mo_3W$ ,  $C_3Mo_2W$ ,  $C_2MoW$ ,  $C_3MoW_2$ , and  $C_4MoW_3$ .

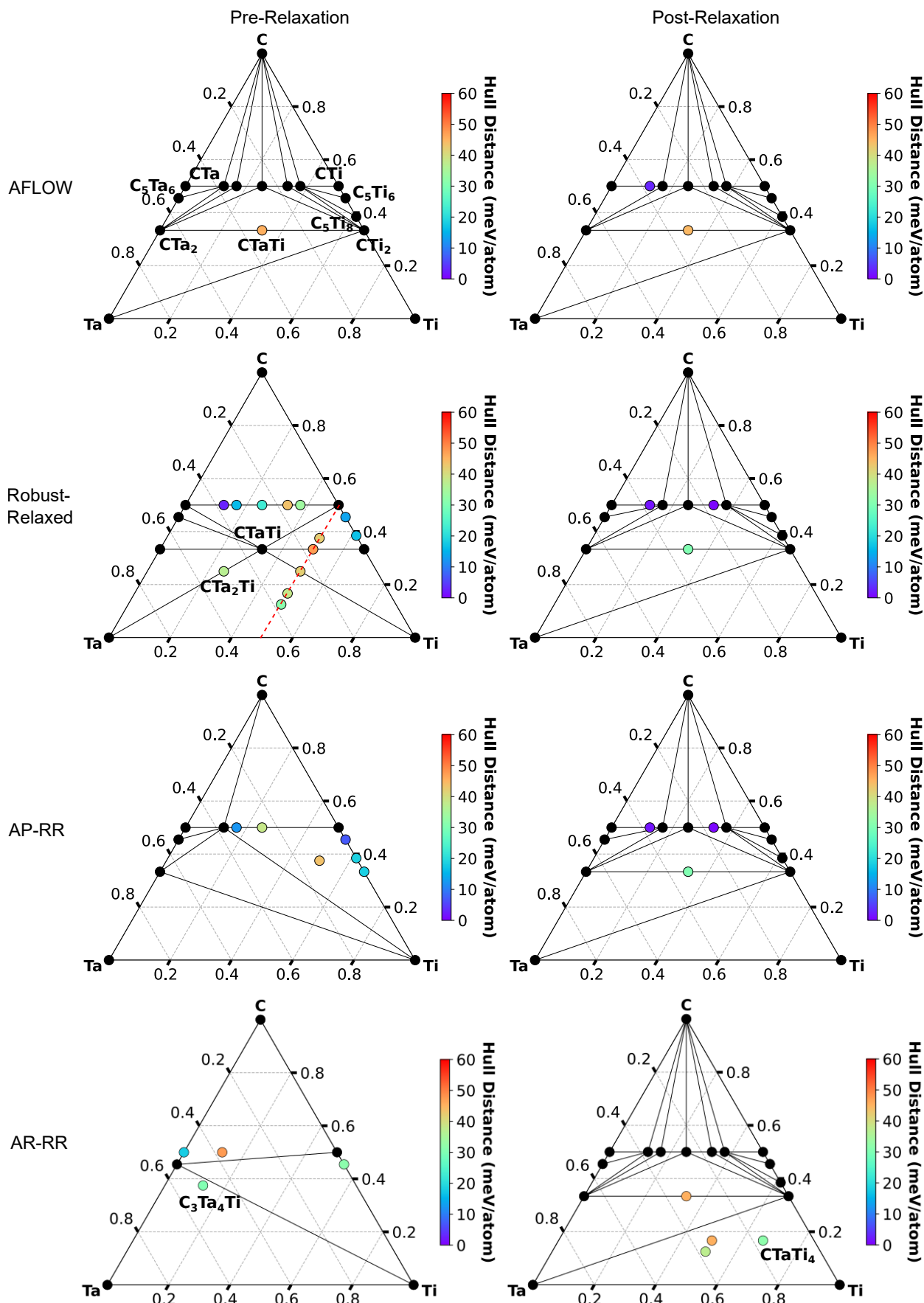


Figure S11: Convex Hulls of CTaTi at Level 10. The unlabeled structures on the line between CTa and CTi are, from left-to-right,  $C_4Ta_3Ti$ ,  $C_3Ta_2Ti$ ,  $C_2TaTi$ ,  $C_3TaTi_2$ , and  $C_4TaTi_3$ . The unlabeled structures on the dotted red line between CTi and TaTi are, from top-to-bottom,  $C_3TaTi_4$ ,  $C_2TaTi_3$ ,  $CTaTi$ ,  $CTaTi_2$ , and  $CTaTi_3$ .

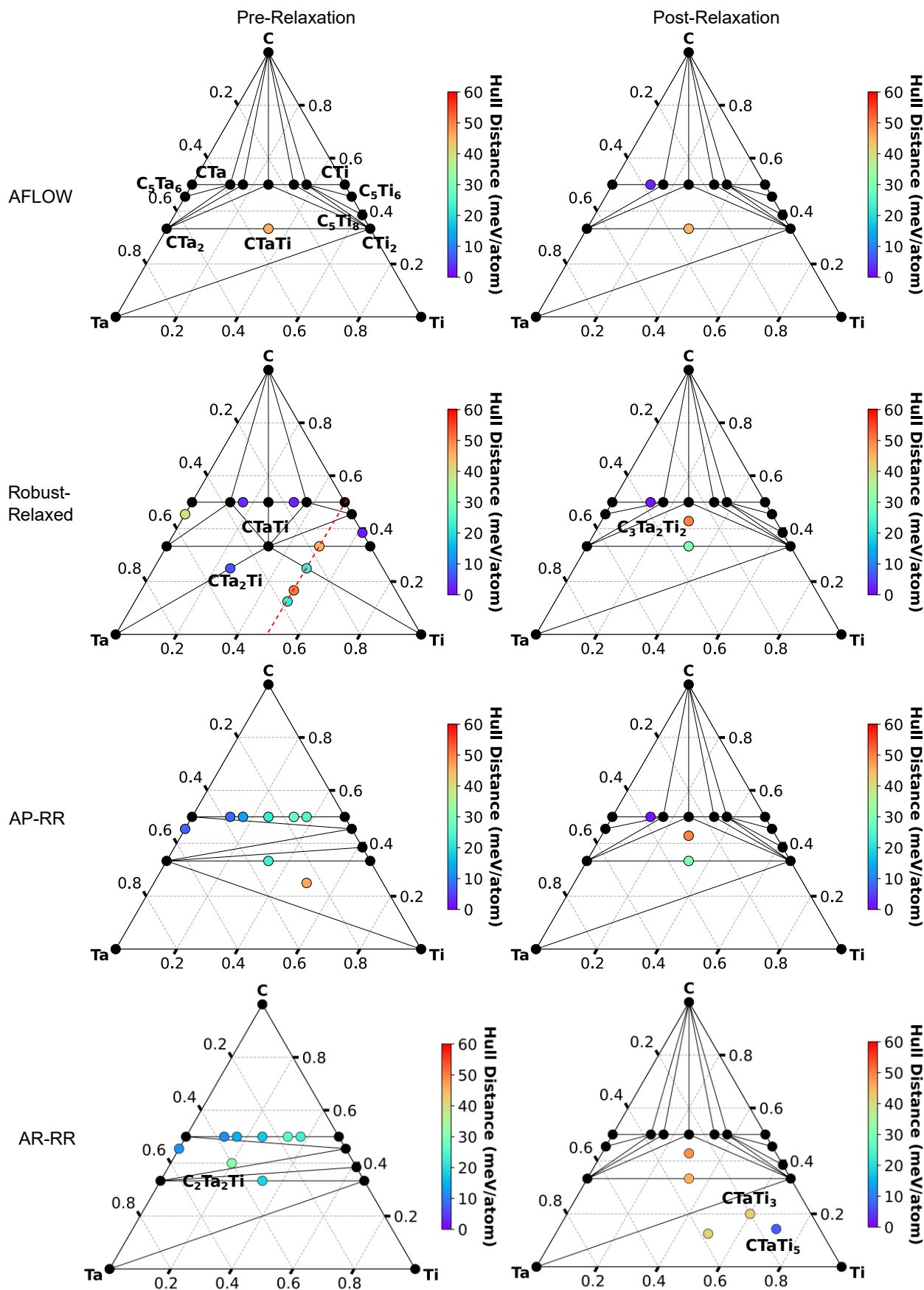


Figure S12: Convex Hulls of CTaTi at Level 16. The unlabeled structures on the line between CTa and CTi are, from left-to-right,  $C_4Ta_3Ti$ ,  $C_3Ta_2Ti$ ,  $C_2TaTi$ ,  $C_3TaTi_2$ , and  $C_4TaTi_3$ . The unlabeled structures on the dotted red line between CTi and TaTi are, from top-to-bottom,  $C_3TaTi_4$ ,  $C_2TaTi_3$ ,  $CTaTi_2$ ,  $CTa_2Ti_3$ , and  $CTa_3Ti_4$ .

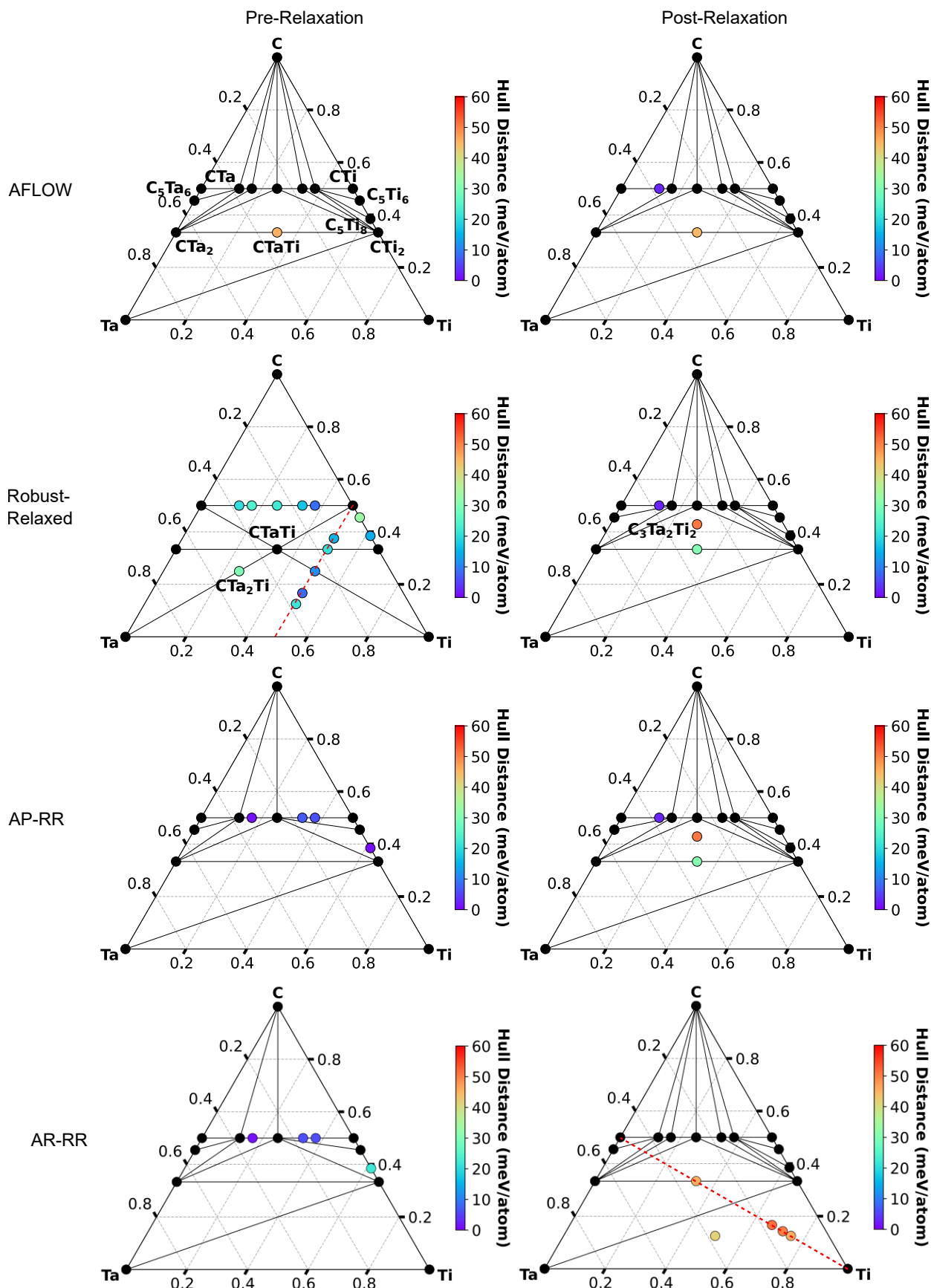


Figure S13: Convex Hulls of CTaTi at Level 22. The unlabeled structures on the line between CTa and CTi are, from left-to-right,  $C_4Ta_3Ti$ ,  $C_3Ta_2Ti$ ,  $C_2TaTi$ ,  $C_3TaTi_2$ , and  $C_4TaTi_3$ . The unlabeled structures on the dotted red line between CTi and TaTi are, from top-to-bottom,  $C_3TaTi_4$ ,  $C_2TaTi_3$ ,  $CTaTi_2$ ,  $CTa_2Ti_3$ , and  $CTa_3Ti_4$ .